

Front page

Exam information

NFYK10020E - Physics Thesis 60 ECTS, Niels Bohr
Institute - Contract:134665 (Christine Wei Andersson)

Handed in by

Christine Wei Andersson
rbg812@alumni.ku.dk

Exam administrators

Eksamensteam, tel 35 33 64 57
eksamen@science.ku.dk

Assessors

Heloisa Nunes Bordallo
Examiner
bordallo@nbi.ku.dk
☎ +4535321215

Hand-in information

Title: Analysis of speckle patterns in coherent small-angle X-ray scattering performed at the European XFEL

Title, english: Analysis of speckle patterns in coherent small-angle X-ray scattering performed at the European XFEL

The sworn statement: Yes

Does the hand-in contain confidential material: No



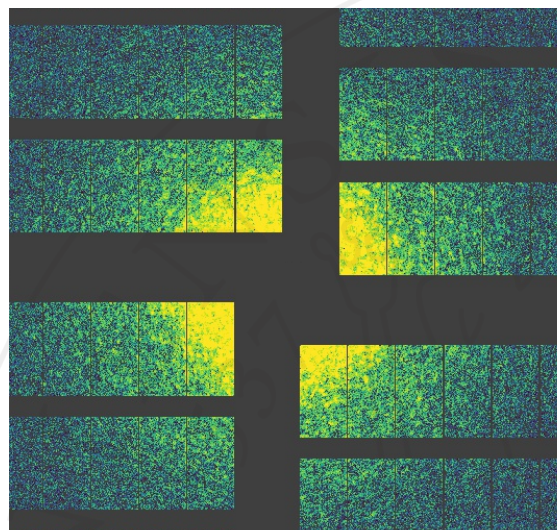
MSc in General Physics

Analysis of speckle patterns in coherent small-angle X-ray scattering performed at the European XFEL

Christine Wei Andersson

Supervised by Anders Madsen and Heloisa Nunes Bordallo

May 2023



Christine Wei Andersson

Analysis of speckle patterns in coherent small-angle X-ray scattering performed at the European XFEL

MSc in General Physics, May 2023

Supervisors: Anders Madsen and Heloisa Nunes Bordallo

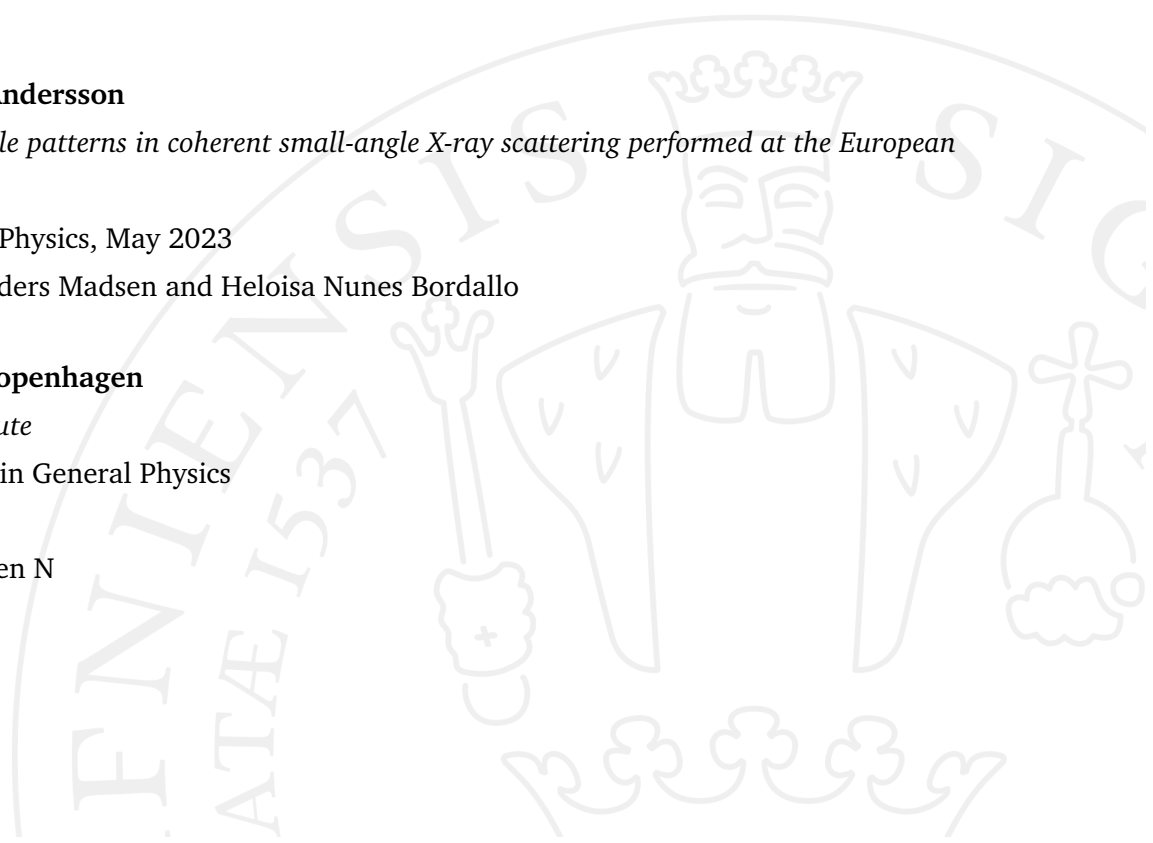
University of Copenhagen

Niels Bohr Institute

Masters Degree in General Physics

Blegdamsvej 3B

2200 Copenhagen N



Abstract

The coherent nature of X-ray Free Electron Laser (XFEL) radiation results in speckle formation during short acquisition times, enabling time-resolved dynamic light scattering experiments like XPCS. These experiments, conducted at a 4.5 MHz FEL repetition rate (available at the European XFEL), offer insights into nano or micro-scale sample dynamics, particularly for timescales between the micro and femtosecond regime. Speckle analysis experiments have the potential to visualize and understand molecular dynamics in various scientific fields such as protein mechanics in biology and strain propagation in solid-state physics, and the presence of resolvable speckles is essential for these studies. Interestingly, the physical size of speckles in reciprocal space is inversely proportional to the spot size of the probing beam. Quantifying this relation would allow for direct recovery of beam size without the need for additional measurements, hence optimizing the experimental setup. With experimental data taken using both dynamic (LUDOX[®] with dynamic timescale $\approx 1 \mu\text{s}$) and static (Vycor) SiO₂ samples at the Materials Imaging and Dynamics (MID) instrument at the European XFEL, this report details the progress made in investigating speckle phenomena in Small Angle X-ray Scattering (SAXS) with the help of X-ray scattering simulations written in Python. The goal of the experiments was to vary the beam size of the incident FEL either by changing its energy or applying nano-focusing optics to study the corresponding speckle patterns obtained from the samples. In addition to performing a SAXS analysis, the spatial intensity autocorrelation function of the scattering pattern was used to characterize speckle size. Results showed an inverse relation between the incident beam and speckle size, supported by simulated data. Additionally, the Rayleigh formalism was applied to describe the XFEL beam's divergence using speckles.

Contents

1	Introduction	1
2	Theory	4
2.1	X-ray Interaction with Matter	4
2.2	Generation of XFEL beams	5
2.3	X-ray Optics	9
2.4	X-ray Scattering	10
2.5	Speckles	12
3	Methods	15
3.1	Experimental data	15
3.2	Simulating speckles	18
3.3	Form factor fitting	21
3.4	Autocorrelation Function	23
4	Results & Discussion	26
4.1	Speckle simulator and SAXS analysis	26
4.1.1	Scattering pattern	27
4.1.2	Experimental SAXS Analysis	29
4.1.3	Porod Analysis	30
4.1.4	Form Factor fitting	32
4.2	Speckle Analysis	36
4.2.1	LUDOX [®] experiment (ΔE)	38
4.2.2	Vycor experiment (NaFo Lens)	40
5	Conclusion	45
6	Bibliography	47
7	Appendix	52
7.1	Github repository	52
7.2	Calculating the diffusion coefficient of 25 nm LUDOX [®]	52

7.3	Calculating the electron density of SiO ₂ and H ₂ O	53
7.4	Fitting of the central peak feature in the y-cut autocorrelation functions for the simulated speckle pattern ROI.	55
7.5	Sasview fitting with various hard-sphere models for 25 nm LUDOX® nanoparticles.	60

Over the past few decades, synchrotron facilities have provided a gateway into understanding the nano-scale structure and dynamics of soft and condensed matter through the scattering of high energy X-rays [1]. In recent years, a new generation of X-ray sources consisting of a linear accelerator (LINAC) rather than a circular storage ring has ushered in a new era of X-ray scattering. Through a process called Self Amplified Spontaneous Emission (SASE), the accelerated electron bunches undergo magnetic dispersion as they experience accelerating forces due to alternating magnetic and electric fields along the undulator path. This causes *microbunching* of the individual electrons in an electron bunch, allowing for the electromagnetic (EM) radiation to radiate constructively in a coherent manner [2].

The machines based on the SASE process are termed X-ray Free-Electron Lasers (XFEL) due to their laser-like coherence properties. Coherent radiation is characterised by a well-defined phase relationship across the wavefront, resulting in a scattered intensity pattern that depends on the spatial distribution of illuminated scatterers. The typical wavelength of XFEL beams ranges from $0.5 - 2.5 \text{ \AA}$ (5 keV–24 keV) [3], making it ideal for probing structures on an atomic length-scale. The photon flux of XFELs is on average 10^5 times greater than 3rd generation synchrotrons (as illustrated in Fig. 1.1) but can have a much larger peak brilliance ($\sim 10^{30}$ photons/s/mm²/mrad²/0.1%BW) [4].

The European X-ray Free-Electron Laser (EuXFEL) in Hamburg, Germany, is the world's first hard X-ray laser facility operating at MHz repetition rate. While synchrotron facilities are limited to X-ray pulses on the length-scale of picoseconds (~ 100 ps), a LINAC makes it fundamentally possible to produce X-ray pulses with a duration as short as 10 femtoseconds (fs) [5], allowing for a variety of time-resolved experiments such as X-ray Photon Correlation Spectroscopy (XPCS). Paired with its high coherence property, the evolution of the spatial distribution of electrons within a

dynamic sample can be studied to quantify any dynamical heterogeneity that occurs both with or without a pump-probe element.

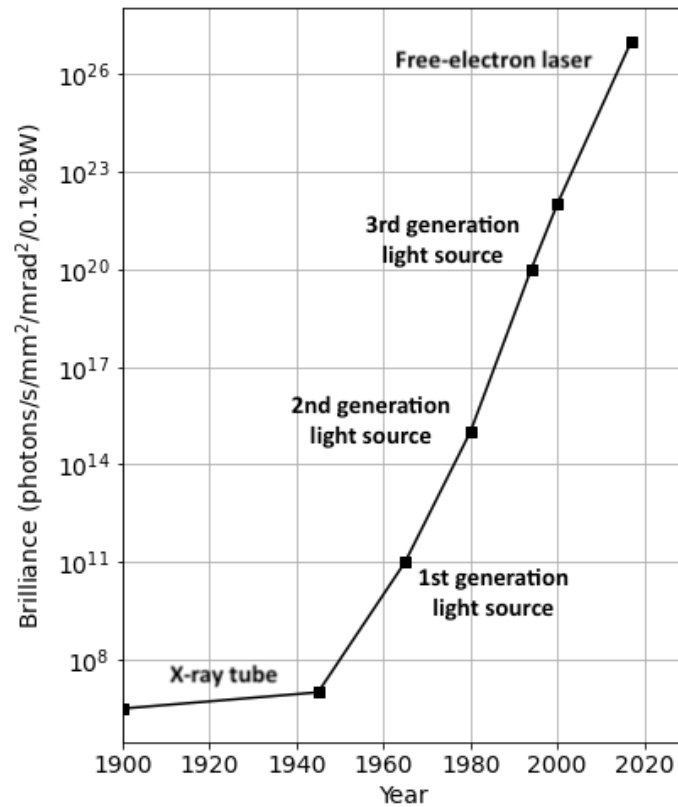


Figure 1.1: Development of the brilliance of emitted radiations from different light sources over the years. For free-electron lasers, we plot the average brilliance. Flux can be used to characterise the number of photons emitted by an SR source. The flux has units of photons/sec/0.1%bandwidth (BW), which is typically $\Delta\lambda/\lambda \approx 10^{-3}$ for XFELs, with λ representing the wavelength. The brightness of the source is characterised as the flux per unit of solid angle of the emitted beam, with units of photons/sec/0.1%BW/mrad². When taking the beam dimension into account, the *brilliance* can be used to define the intensity. It is simply the brightness per mm² of the source size. (Adapted from Jens Als Nielsen's *Elements of Modern X-ray Physics* [4].)

Diffraction-before-destruction is a further feature of scattering experiments with XFEL. Biological samples are extremely sensitive and undergo coulomb explosion when exposed to ionising radiation such as high energy density X-rays [6]. With fs pulses the state of the molecule both before and after the destruction can be probed and studied, which allows experimenters to evade the radiation damage, all without the expense of flux due to the brilliance of FELs. In the case of a ps pulse, the destruction time could be much shorter and the results would only reflect the aftermath of the interaction. At EuXFEL time-resolved measurements of molecular

dynamics, lattice strain determination under extreme conditions, and single-particle scattering images are now achievable goals [7].

Scattering experiments performed with coherent XFEL radiation have resulted in the experimental phenomena known as *speckles*, which have been studied at large in the application of visible laser light but are still novel in synchrotron light source facilities. Speckles occur when the reflected or diffracted light interferes to produce small variations in the intensity of the diffracted pattern and are often visually described to resemble noise grains. To resolve speckles, the difference in the scattered radiation's path lengths must be smaller than the longitudinal coherence length of the incident beam [8]. For a highly ordered sample, the scattered intensity displays dominating Fourier frequencies like Bragg reflections. For a sample of randomly spatially distributed scatterers, the relative position of the scatterers, as well as the number of emitters within a sample, do not affect the size of speckles in a diffraction pattern [9]. In fact, it is only the width of the incident beam size that has a direct inverse relation to the speckle size.

In this thesis, theoretical results obtained from a speckle pattern simulator as well as experimental data taken at the Materials Imaging and Dynamics (MID) instrument at EuXFEL are used to characterise the relationship between incident beam width and speckle size by autocorrelating the images. So far synchrotrons and XFELs mainly use wire scan systems or screens to profile beam size [10]. However, as XFEL radiation varies slightly in property from pulse to pulse [2], only a general beam size can be concluded with such techniques if the XFEL beam does not destroy the material first. If beam size can be recovered through speckle analysis, the illumination size of individual pulses can be quantified without requiring any additional experimental procedures, which could become important in fast beam dynamic behavior investigations. Being able to precisely recover experimental conditions, like the beam width, by analysing speckle size in diffraction patterns would allow for faster development in the operations and machine abnormality studies at XFEL.

Furthermore, with a more sophisticated characterization and comprehension of speckles, XPCS analysis where X-rays instead of visible light is utilized in the context of Dynamic Light Scattering (DLS) experiments [11] can be refined to improve results obtained in both small and wide angle configuration. For example, a colloidal suspension exhibiting Brownian motion on a characteristic timescale on the order of $10 \mu\text{s}$ (see Sec.7.2) would have highly resolvable dynamics studied under EuXFEL's fs radiation exposure time. Critical fluctuations near phase transitions in fluids can also be realised with experimental data using XFEL beams.

2.1 X-ray Interaction with Matter

Electromagnetic (EM) radiation can be used to study and resolve meso and nano-scale objects in experimental physics [Scheffold and Cerbino]. To study objects on a nanoscale, such as proteins and crystal lattice structures, we would need wavelengths of similar order ($10^{-8} - 10^{-12}$ m), which falls in the range of X-ray radiation. The energetics of EM radiation has the following relation between energy E and wavelength λ :

$$\lambda[\text{\AA}] = \frac{hc}{E} = \frac{12.4}{E[\text{keV}]}, \quad (2.1)$$

where h is Planck's constant and c the speed of light. The index of refraction describes how the propagation of EM radiation changes with varying material and is given by [12]:

$$n = 1 - \delta + i\beta. \quad (2.2)$$

The real and imaginary parts describe the photon refraction (δ) and attenuation (β) and can be rewritten as:

$$\delta + i\beta = \frac{r_e \lambda^2}{2\pi} \rho_{at} f = \frac{r_e \lambda^2}{2\pi} \rho_{at} (f_1 - i f_2), \quad (2.3)$$

where $r_e \approx 2.817 \times 10^{-5}$ Å is the classical electron radius and ρ_{at} the atomic density. The atomic scattering factor $f = f_1 - i f_2$ represents the dispersion and attenuation of photons, respectively. As radiation energy increases, f_1 approaches the number of electrons per atom and $\rho_{at} f_1 \rightarrow \rho_e$, the electron density [12].

For X-rays, the real part of the refractive index is slightly smaller than unity. Therefore, to focus the beam, concave lenses are used instead of typical convex lenses. δ is typically on the order of 10^{-5} [13], and decreases with increasing X-ray energies $\delta \propto \lambda^2$. For decreasing δ , $n \rightarrow 1$ and the beam is less focused.

The dominating X-ray and matter interaction process is photoelectric absorption for photon energies $\lesssim 50$ keV (see Fig. 2.1) and high Z materials [14]. When an XFEL beam illuminates a scattering volume, the important scattering process is Thomson and Rayleigh scattering, in which no energy is lost during the process and the scattered light is coherent. There is also a definite phase relationship between the incident and scattered beam [15]. In some cases, a loosely bound electron can absorb a fraction of the incident photon's energy causing inelastic scattering (Compton scattering). The scattered light has a longer wavelength and is considered incoherent. In these experiments, the inelastic scattering contributes to a background diffraction pattern which can reveal structural and dynamic information similar to coherent scattering but is unwanted in speckle experiments.

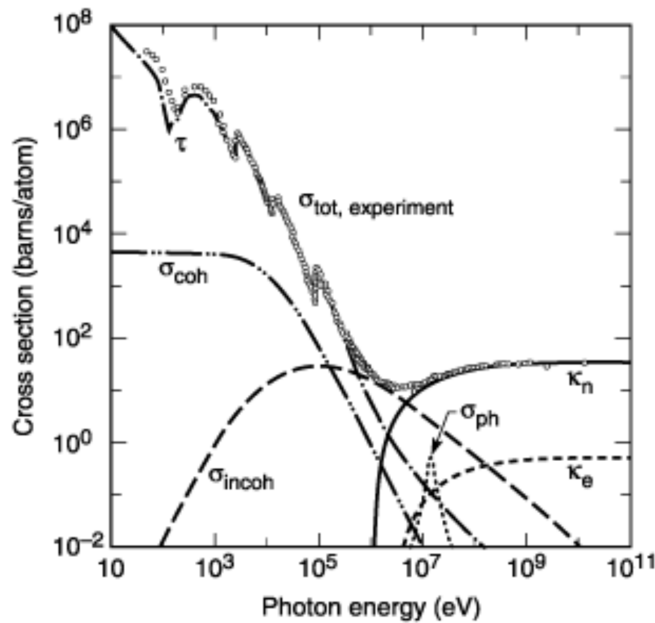


Figure 2.1: Photon cross section of lead (Pb) as a function of energy. The total photon cross section is expressed as σ_{tot} (circular markers), with individual contributions from photoelectric absorption τ , coherent/Rayleigh scattering σ_{coh} , incoherent/Compton scattering σ_{incoh} , photonuclear absorption σ_{ph} and electric κ_e and nuclear κ_n pair production (Reproduced from J. H. Hubbell [16], with the permission of AIP Publishing).

2.2 Generation of XFEL beams

Although first, second, third, and fourth-generation synchrotrons rely on circular storage rings to produce high-energy X-rays, XFEL facilities such as EuXFEL in Hamburg, Germany, use LINACs to achieve higher electron energy and radiation brilliance. While circular storage ring-based fourth-generation synchrotron facilities such as the MAXIV laboratory in Lund, Sweden, can produce X-ray radiation up to

10^4 keV with a brilliance at least one order of magnitude higher than third-generation synchrotrons [17], EuXFEL can deliver up to 100 million times more brilliance with an electron energy of 17.5 GeV and a higher degree of transverse coherence [18].

The production of FELs starts upstream of a linear tunnel stretching 3.5 km from the experimental hutches at EuXFEL [18]. The injector, located at the DESY campus in Hamburg, Germany, consists of a solid cathode that emits bunches of electrons when excited by a laser. The bunch is accelerated to 120 MeV using an electron Radio Frequency (RF) gun and gets directed into a 1.6 km long LINAC. The LINAC consists of three main RF cavity stations using synchronised oscillating electric fields to accelerate the passing electron bunches. Two bunch compressors, one located after the first RF station (electron bunch at 0.5 GeV) and one after the second (electron bunch at 2.0 GeV), aid in driving up the current of the electron bunch in order to reach an energy of 17.5 GeV before exiting the accelerator. With the ability to accelerate a large number of electron bunches per RF period, the beamlines at EuXFEL can work with an impressive X-ray pulse repetition rate. Figure 2.2 illustrates the X-ray train and pulse structure. For 17.5 GeV, the trains containing individual X-ray pulses are delivered at a rate of 10 Hz, with each train containing up to 2700 pulses (4.5 MHz per train) [18].

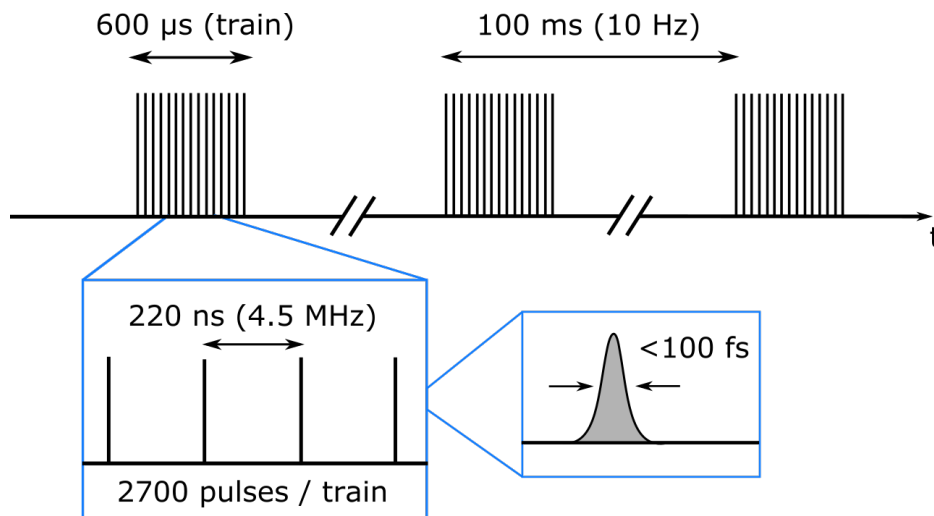


Figure 2.2: Photon beam structure at the EuxFEL with pulses of X-rays delivered in trains at a rate of 10 Hz. Each train contains a pulse rate up to 4.5 MHz with a $\Delta t = 220$ ns spacing between single pulses.

At almost the speed of light, the electrons get directed into a notably long undulator where X-ray radiation is produced through a free-electron process called Self Amplified Spontaneous Emission (SASE). An undulator is an insertion device common in third generation light source facilities that contain periodic magnetic dipoles (see Fig. 2.3) that induce spontaneous emission of X-rays from passing electrons

[7], due to transverse acceleration from the Lorentz force applied by the magnetic fields. Located underground in the electron tunnel, the SASE-2 undulator produces XFELs for multiple beamlines operating at EuXFEL, namely the Materials Imaging and Dynamics (MID) and High-Energy Density (HED) stations [5]. Consisting of 35 consecutive 5 m long variable-gap components, the 175 m SASE-2 undulator is able to produce hard X-rays ranging from 5 to 25 keV.

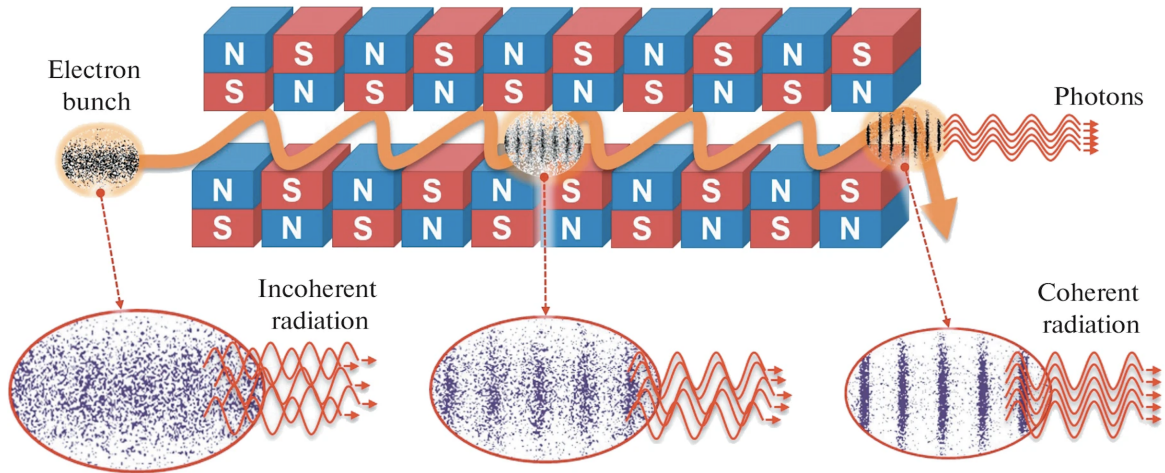


Figure 2.3: Illustration of the Self Amplified Spontaneous Emission (SASE) process in an undulator courtesy of M. V. Kovalchuk & A. E. Blago, taken with the permission of Springer Nature Publishing [19].

As EM light always travels faster than the electrons, when the radiation is ahead of the electrons by a distance λ , a resonant condition is met where the EM field produced by the moving charges in one part of the electron bunch create an instability in the moving charges in another part of the bunch. This instability modulates the electron density along the undulator to achieve complete microbunching, as illustrated in Figure 2.3. For an electron bunch without a microstructure, the radiation power is proportional to N . In the case of microbunching, the radiation power scales with N^2 as the radiation field is self amplified through coherent emission [18]. At the end of the undulator, the electrons are stopped at the beam dump and the radiation continue towards the photon tunnels.

Although XFELs are considered chaotic sources based on spontaneous emission, a near laser-like coherence is created with the SASE process and improved with adequate beam apertures and bandwidth selection using monochromators. Figure 2.4 shows a comparison of the typical energy spectra of an XFEL with that of a visible light laser. Similarities can be observed in terms of the harmonic modes of emission and in both cases the bandwidth remains below 10^{-2} . For an unfiltered XFEL beam, also known as the “pink beam”, the energy bandwidth is on the order of 10^{-3} keV.

Using Si(111) and Si(220) monochromators narrows the bandwidth of the FEL down to the order of 10^{-4} and 10^{-5} respectively.

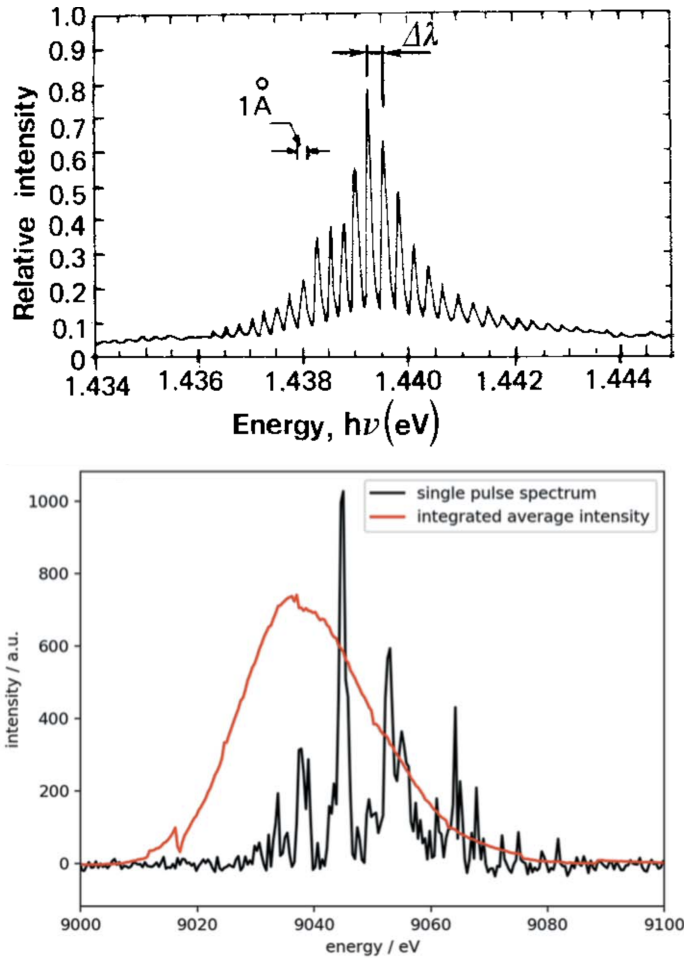


Figure 2.4: Comparison of typical spectral emissions for *Top*: a semiconductor laser (figure courtesy of O. Svelto [20]), and *Bottom*: a single-shot [black line] and average shot [red line] SASE XFEL (figure courtesy of A. Madsen et al. [5])

The main difference between the two (other than their energies) is that visible laser light is oscillated within a reflective cavity, creating standing waves that purify the spectra, and the result is stimulated emission where the phase can be well defined at any point. XFEL beams are produced in a single run-through process that results in the spontaneous emission of short discrete pulses of radiation. Thus, for XFEL beams, the spectra is not as well defined and vary slightly with each pulse. While the transverse coherence of XFEL beams is excellent, the longitudinal coherence length is limited by the spectral bandwidth $\Delta\lambda/\lambda$ through the following formula [2]:

$$l_l = \frac{\lambda}{2\Delta\lambda/\lambda} \quad (2.4)$$

2.3 X-ray Optics

Due to their laser-like properties, it is reasonable to assume that XFEL beams follow the same physical principles as visible laser light. The main type of optics used for focusing the X-rays are Compound Refractive Lens (CRLs) made of the stable low- Z element Beryllium (Be) for minimum absorption and scattering [21]. The melting point of Beryllium is also moderately high (1287 °C) [22], giving it good strain resistance against the XFEL beam.

The simple lens formula that describes the relationship between focal length f , the distance between the source and the lens p , and distance between the lens and the sample q , is given by [23]:

$$\frac{1}{f} = \frac{1}{p} + \frac{1}{q}. \quad (2.5)$$

If $p = \infty$ or $p \gg q$ (which is the case for XFEL since the source is about 1 kilometer away from the lenses, and the lens to sample distance is 30 cm), then Eq(2.5) becomes $f = q$.

In optics, a beam with a Gaussian-distributed amplitude envelope in the transverse direction is considered a Gaussian beam. If the transverse coherence length is greater than or equal to the beam size (full transverse coherence), the beam is also considered diffraction limited, where the minimum beam width is restricted only by the diffraction properties of the radiation. Since an XFEL beam has complete transverse coherence, we can assume the following applies to beam properties at EuXFEL beamlines.

The radius of a Gaussian beam's spot size after focusing is defined by the beam width, $w(z)$, and depends on the position, z , centered at the focal point along the direction of radiation propagation [24]:

$$w(z) = w_0 \sqrt{1 + \left(\frac{z}{z_R}\right)^2}. \quad (2.6)$$

Schematically shown in Figure 2.5, w_0 is the minimum spot size at $z = 0$. As XFEL beams are diffraction limited [25], we can only expect the beam size to decrease linearly with distance until $w(z) \approx \sqrt{2}w_0$, whereby the evolution of beam size follows Eq.(2.6). The regime under which this holds true is determined by the Rayleigh length [24]:

$$z_R = \frac{\pi w_0^2}{\lambda}, \quad (2.7)$$

which depends on the wavelength of the beam as well as the minimum beam radius.

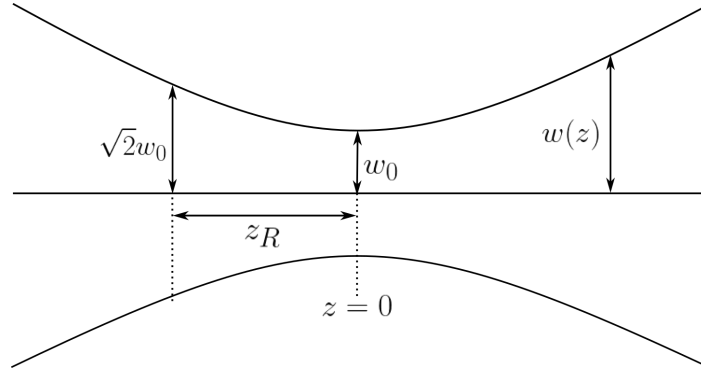


Figure 2.5: Beam width $w(z)$ of a Gaussian laser beam as a function of the propagating direction z . At the focal point $z = 0$, the beam waist is w_0 , and the Rayleigh length z_R is indicated.

The smallest beam width, w_0 , at position $z = 0$, is then located at a distance q downstream of the focusing lens. A sample placed at that position is illuminated by the smallest possible beam size, while moving the sample Δz further upstream or downstream increases the volume of illumination.

2.4 X-ray Scattering

Small-angle X-ray Scattering (SAXS) is an experimental technique employing the interaction of hard X-rays with matter to probe the distribution of electrons within a sample on the nano or meso-scale. The electrons scatter the incident photons elastically, acting as spherical wave sources, which then interfere to create a diffraction pattern. Similarly to how the diffraction pattern of a Young's double slit experiment performed with coherent laser light can reveal the distance between grating slits [26], the scattering pattern of a SAXS experiment can reveal the structural form of soft and nano-scale matter. This is because the combined coherent scattering amplitude carries information about the distribution of scattering electrons with spatial preservation. Although the phase and amplitude is unrecoverable in an experiment, the squared modulus of these terms is realised in the form of a scattering pattern, detectable with a photosensitive detector.

The scattering pattern, $I(Q)$, is measured in terms of intensity and is often expressed as a function of momentum transfer, Q :

$$Q = |\mathbf{k} - \mathbf{k}'|, \quad (2.8)$$

where \mathbf{k} and \mathbf{k}' are the incident and emergent wave vectors respectively. For elastic scattering: $|\mathbf{k}| = |\mathbf{k}'| = 2\pi/\lambda$. The magnitude of the momentum transfer is related to the scattering angle, 2θ through [4]:

$$Q = 2|\mathbf{k}| \sin \frac{2\theta}{2} = \frac{4\pi}{\lambda} \sin \frac{2\theta}{2}, \quad (2.9)$$

where the wavelength, λ , is inversely proportional to Q . The shorter the wavelength, the larger the momentum transfer. Similarly, the greater the scattering angle, the greater the momentum transfer. A schematic diagram of a standard SAXS experimental set-up is illustrated in Figure 2.6.

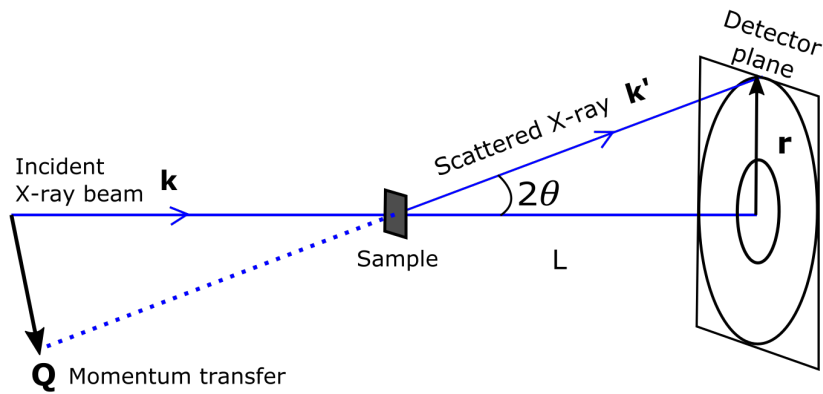


Figure 2.6: Schematic representation of a typical scattering experiment with a sample placed at a distance L from the detector plane. The incident and scattered beams are represented with their respective wave vectors \mathbf{k} and \mathbf{k}' with a scattering angle of 2θ . The resultant momentum transfer \mathbf{Q} is illustrated, as well as the distance r of the detected photon from the center of the detector.

The scattering amplitude in small angle scattering is nothing else than a Fourier Transform (FT) of the electron charge density, $\rho(\mathbf{r})$. The FT of a scattering volume is visualised with the reciprocal space. The reciprocal space, also called the Fourier space, is mathematically conceptualised with an infinite number of periodically repeating reciprocal lattices. The spacing between each reciprocal lattice point is inversely related to the smallest resolvable distance in real space, d with $Q = 2\pi/d$ [27]. If the distances in real space have a dimension of length L , in reciprocal space the unit would be L^{-1} .

For a single atom, the scattering amplitude within a radius of $|\mathbf{r}|$ from the center of the atom is represented by [4]:

$$F^0(\mathbf{Q}) = \int \rho(\mathbf{r}) e^{i\mathbf{Q}\cdot\mathbf{r}} d\mathbf{r} . \quad (2.10)$$

For $Q \rightarrow 0$, $F^0(\mathbf{Q}) = Z$ as the integral should equal the total number of electrons in the atom, and for $Q \rightarrow \infty$, $F^0(\mathbf{Q}) = 0$. Since the scattering amplitude is a complex number, when referring to the scattered intensity pattern, the absolute square of the scattering amplitude is taken to remove the imaginary phase contribution [28]:

$$I(Q) = |F(Q)|^2 . \quad (2.11)$$

Often times the scattering intensity is also called the *form factor*, which is the mathematical representation of the density distribution of electrons in reciprocal space.

For an arrangement of isolated particles suspended in a solvent, meaning any inter-particle interactions can be neglected, the form factor takes a similar form to the atomic form factor (Eq.(2.10)) except the electron charge density $\rho(\mathbf{r})$ is replaced by the scattering contrast density $\Delta\rho = (\rho_p - \rho_s)$, where both the particle and solvent are assumed to have uniform scattering length densities:

$$F(\mathbf{Q}) = \frac{1}{V_p} \int_{V_p} \Delta\rho e^{i\mathbf{Q}\cdot\mathbf{r}} dV_p . \quad (2.12)$$

From this, it is apparent that the form factor depends on the size and shape of the particle as the integral is performed over the volume of the particle, V_p . A general expression for the scattering intensity of suspended particles could then be [29]:

$$I(\mathbf{Q}) = N_p V_p^2 |F(\mathbf{Q})|^2 \quad (2.13)$$

where the intensity is also weighted by the number of particles, N_p in the sample. To analyse these equations numerically can prove challenging depending on the required parameters within the integral. One simple case is the scattering intensity for a monodisperse sample of spheres, which is discussed later in Section 3.3.

2.5 Speckles

Going back to drawing upon similarities between XFEL radiation and visible laser light, Goodman describes in his book: *Speckle Phenomena in Optics*, that speckles arise as a consequence of constructive and destructive interference from fine-scale

differences in the path length of scattered X-rays [8]. As such, a vital condition for the observation of speckles is that the longitudinal coherence length (Eq.2.4) of the incident beam is longer than the size of fluctuations in the scattered radiation's path lengths. The longitudinal coherence length of XFEL beams are long enough for high contrast resolvable speckles to manifest in SAXS experiments [25], at wide-angle configurations, speckle visibility becomes increasingly challenging due to larger path lengths at higher angle.

The measured intensity exhibits granular noise that has a direct correlation to the spatial positioning of the scatterers. The number of scatterers does not affect the characteristics of the speckles [9], instead, it is the volume of illumination that affects the size of the speckle granules, which is determined by the spot size of the beam. Therefore, developing an understanding of the nature of speckles in XFEL experiments can lead to new ways of characterising beam profiles.

In the case of a dynamic sample, the change in the spatial orientation of atoms and electrons will result in a change in the spatial orientation of speckles in our scattering image. XPCS experiments are then possible under the condition that the characteristic timescale of the dynamics of the sample is longer than the exposure time of the scattering image. The spatial evolution of speckles with time then contains information regarding structural changes within the sample. For EuXFEL's 4.5 MHz repetition rate, single-shot images corresponding to one pulse of radiation will result in a scattering pattern with visible speckles, similar to the left half of Figure 2.7. For an image acquisition time longer than the dynamic timescale of the sample, the speckles become washed out and the SAXS pattern only contains information related to the form factor. This is displayed on the right side of Figure 2.7, where the image is averaged over 50 consecutive single-shots.

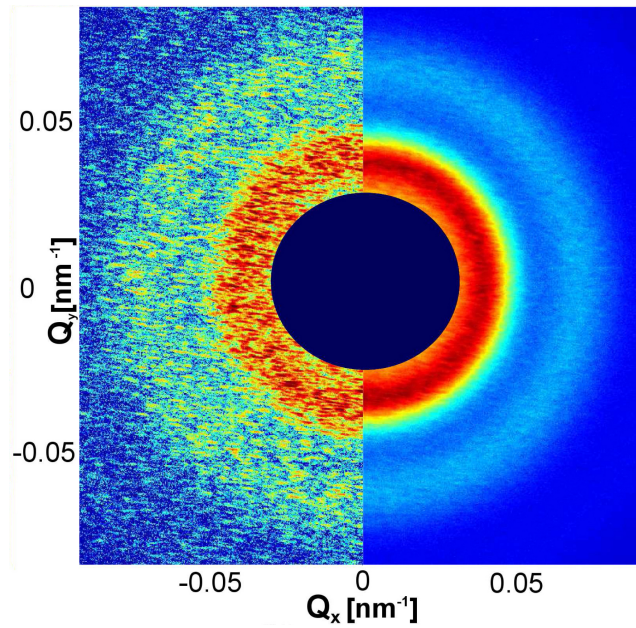


Figure 2.7: X-ray scattering pattern from a colloidal sample. On the left, a coherent pattern from a single-shot image is displayed, revealing notable spatial intensity fluctuations. On the right half of the image, the scattering ring generated from the summation of 50 consecutive shots is exhibited. The circular shadow at the center of the image is caused by the beam stop, which obstructs the direct beam from reaching the detector. (Figure modified from Soohyong Lee et al [30])

3.1 Experimental data

The SAXS experiments were conducted at the Materials Imaging and Dynamics (MID) station at EuXFEL. The X-ray pulses are delivered in “trains” operating at a repetition rate of 10 Hz. As shown in Figure 2.2, each train consists of up to 2,700 pulses and a repetition rate of 4.5 MHz. This means that MID can deliver 27,000 pulses/second.

In our experiment, we used a repetition rate of 2.25 MHz [5]. Depending on the experimental conditions, the energy of the X-ray beam can be tuned within a range of 5 to 25 keV. Two silicon monochromators Si(111) and Si(220) are situated after the SASE2 undulator and optics hutch but were not required in this case. The pink beam was used with a bandwidth of 10^{-3} keV. Each single-shot image is labeled with a pulse ID and train ID number.

MID has three main experimental configurations illustrated in Fig. 3.1: Large field-of-view (LFOV) ($2\theta \leq 23^\circ$), Wide-angle X-ray scattering (WAXS) ($14^\circ \leq 2\theta \leq 55^\circ$) and SAXS ($2\theta \leq 14^\circ$) - which is the configuration used for our experiments. Each of these configurations in the experimental hutch is illustrated in Fig. 3.1. While speckle analysis is of interest in both small and wide-angle scattering, the characterisation of speckles can be better analysed in the SAXS configuration where the data obtained has considerably higher intensity and distinguishable speckle patterns. In addition, for analysis in WAXS configuration, a detector with a smaller pixel resolution and higher photon sensitivity would be required to provide enough speckle contrast as well as good resolution for image analysis since speckles can get as small as standard SAXS detector pixels.

An Adaptive Gain Integrating Pixel Detector (AGIPD), which consists of 16 modules (512×128 pixels each) forming 4 motor-controlled quadrants, is used to measure the intensity of scattered light. The pixel resolution is $200 \mu\text{m} \times 200 \mu\text{m}$, with a high range of photon sensitivity ranging from one to 10^4 photons [31]. For our SAXS experiments, the detector was placed at a distance of 7.9 m away from the sample using the adjustable Large Detector Arm (LDA).

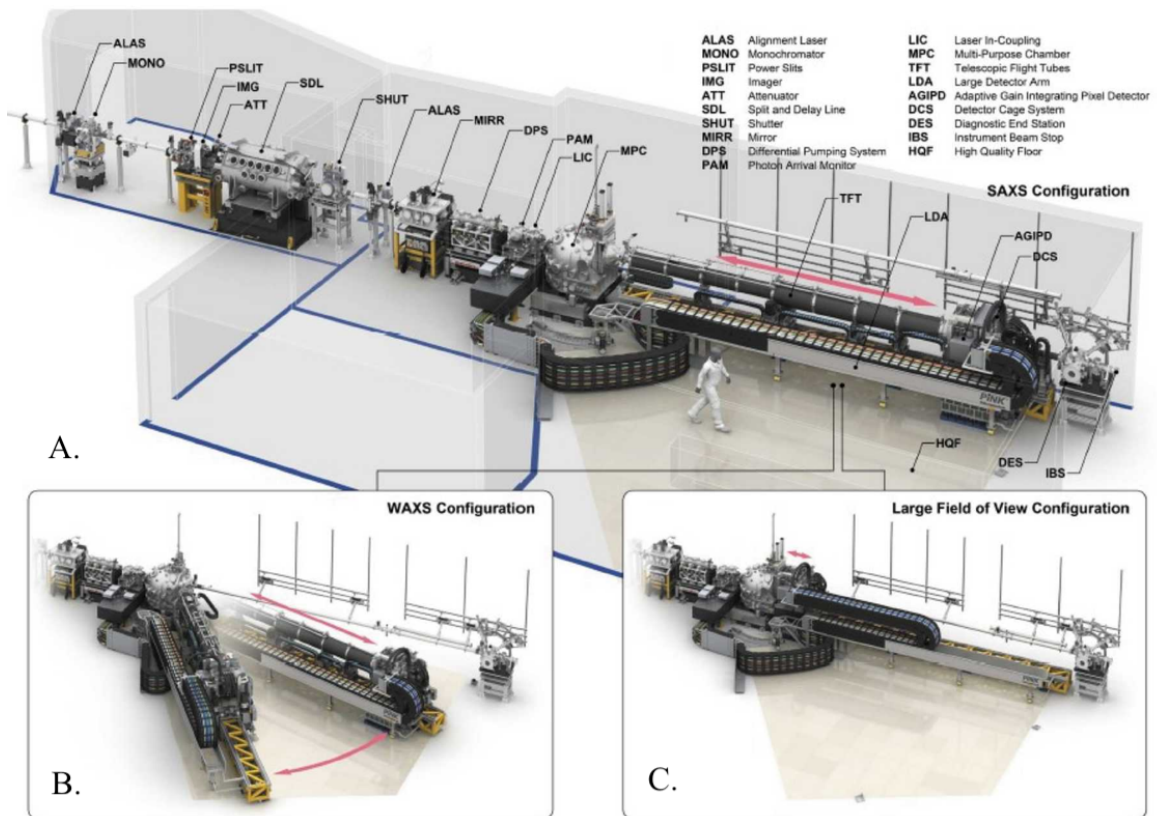


Figure 3.1: 3D CAD-model of MID's optics and experiment hutch. Components are individually labeled including insets of the detector arm in various experimental geometries: A) SAXS configuration. B) WAXS configuration. C) Large Field of View configuration. Modified from: European XFEL/Rey.Hori [5]

Two experiments with different Si samples were used to obtain speckle data. In the first experiment, our independent variable is the energy of the incident beam. From Eq.(2.2) and (2.3) in the theory of X-ray interaction with matter, we know that increasing the energy of the photons causes the refractive index n to decrease. Combining with Eq.(2.5), we can observe how the focal length is dependent on the energy of the beam: $f \propto \frac{1}{\delta} \propto \frac{1}{\lambda^2} \propto E^2$. Thus, by increasing the beam energy, we expect to notice an evolution in the size of the speckle patterns. Figure 3.2 provides an illustration of how the focal point z_0 , and thus the beam size at the sample, changes for varying energy. The photon energy of the FEL beam was changed in discrete steps of 0.1 keV from 8.7 keV to 9.2 keV, and the scattered intensities were recorded.

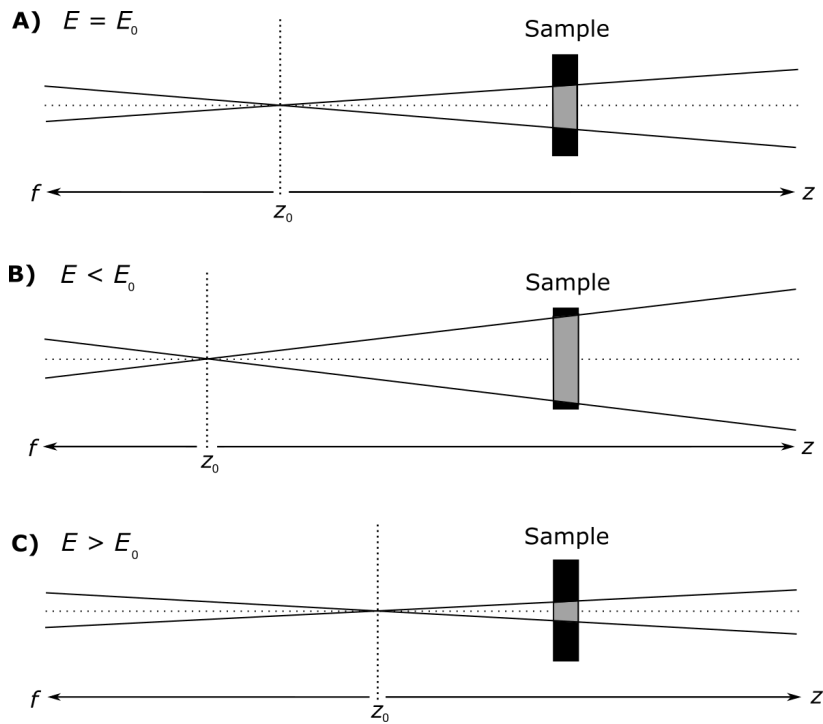


Figure 3.2: Schematic diagram illustrating the change in beam width at the sample when applying a change in energy to the beam that is focused before the sample at position z_0 . **A)** Beam is focused at position z_0 before the sample with a specific beam width at the sample position. If the sample is downstream of the focal point as in the figure, decreasing the energy shortens the focal length of the beam increases the beam width at the sample (**B**), while increasing the energy increases the focal length, which in turn decreases the beam width (**C**).

A colloidal suspension of spherical LUDOX[®] Silicon dioxide, SiO_2 , nanoparticles ($R = 25 \text{ nm}$) was chosen as our sample. Since the experimental data is related to the structure of the individual particles, a sample of monodisperse spheres produces easily analysable (familiar and distinguishable) results that allow us to focus on experimental and data features related to the speckles. Silica particles have a high electron density compared to water. For SiO_2 nanoparticles suspended in water, the electron density of the spheres is ≈ 2.4 times that of water (see Sec. 7.3), so our sample ensures a good contrast to observe the scattering from the spheres. Keeping in mind that a single train spans $600 \mu\text{s}$ and contains 2700 pulses, with a diffusion coefficient of $0.905 \times 10^{-11} \text{ m}^2/\text{s}$ which translates to a μs dynamics timescale (see Sec. 7.2), we expect the speckles to get washed out when averaging over more than 5 single shot images. For analysis related to the structure of the sample (modeling of the form factor), we can simply average over multiple shots to get a high-intensity pattern. For analysis of speckles, single-shot images (corresponding to 2.25 MHz X-ray pulses on the sample) are used.

For the second experiment, we kept the energy of the X-ray at 9 keV and opted to insert CRLs to adjust the beam width. A NanoCRL Focusing (NaFo) lens was placed 30 cm before the sample in the experimental hutch along the beam's direction of propagation, z . Computer-controlled motors were used to adjust the position by ± 10 mm in steps of 100. According to Eq.(2.5) the focal point is dependent on the position, q , of the NaFo lens. Taking Eq.(2.6), we can substitute z for $z - z_0$:

$$w(z) = w_0 \sqrt{1 + \left(\frac{z - z_0}{z_R} \right)^2}, \quad (3.1)$$

where z_0 is the position of the NaFo lens that sets the focal length at the position of the sample ($f = q$) and $w(z_0) = w_0$.

As NaFo lenses create small focused beams, a highly concentrated amount of radiation is deposited to the sample, which in the case of LUDOX[®] would cause excess heating and sample destruction. To avoid this, we used a 10 nm Vycor glass sample produced by EuXFEL collaborators at the Technical University of Hamburg (TUHH). Vycor is a high thermal resistant glass composed of 96% SiO₂ and 4% Boron trioxide, B₂O₃ [32]. Notably, Vycor has a temperature resistance of up to 900°C, making it an excellent choice for this experiment where we intend to measure the smallest achievable beam size with our set-up. Vycor glass is produced by soaking the material in acid, which dissolves the B₂O₃ and forms porous cavities within the silica glass that act as scatterers. The sample thickness is about 20 μ m and has a porosity of $\sim 70\%$.

3.2 Simulating speckles

Simulations help provide theoretical results that can aid in the comparison of experimental results. To obtain some expected results for our experimental data, we simulated the scattering pattern of our first sample - a spherical monodisperse nanoparticle sample ($R = 25$ nm). The simulation and computational analysis were written in Jupyter Notebooks using Python code that can be found in Ref. 7.1.

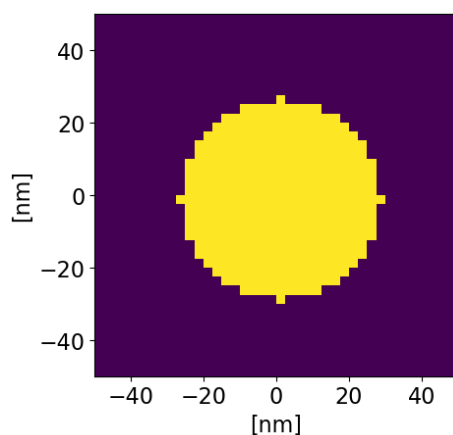


Figure 3.3: A single 25 nm circular nanoparticle with pixel value 1 simulated on an null matrix.

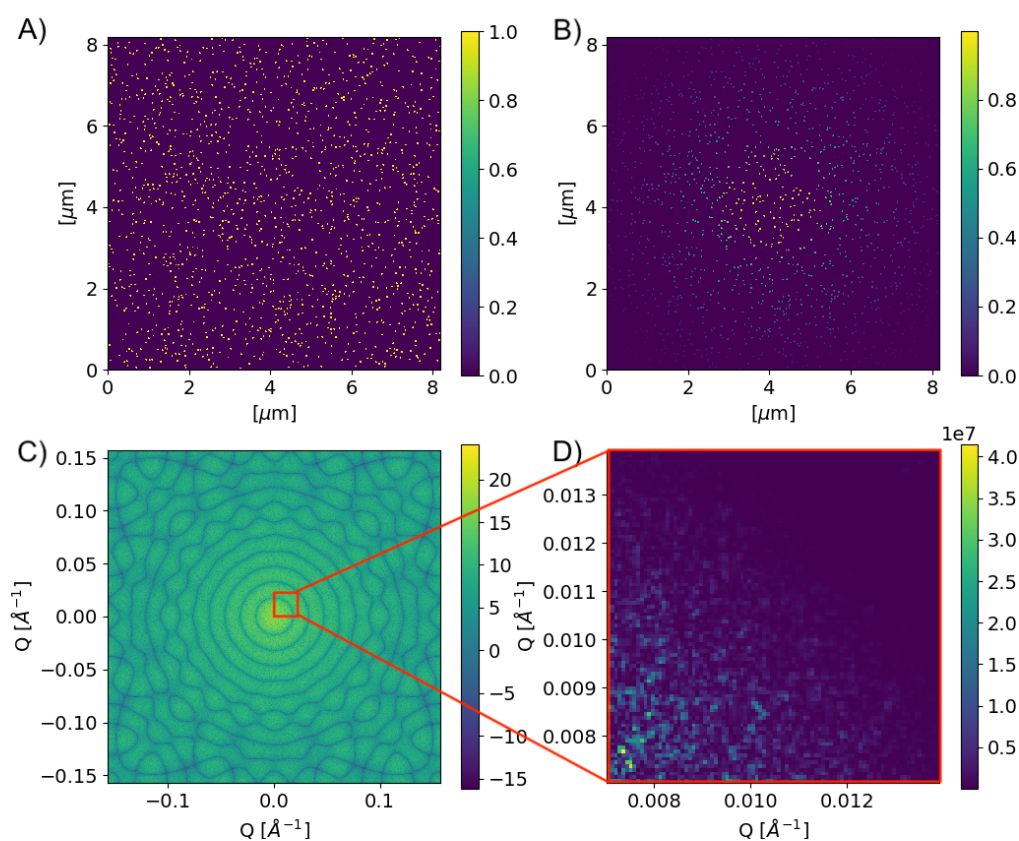


Figure 3.4: **A)** Randomly generated 4096×4096 matrix sample image with 1500 particles ($R \approx 25$ nm) and a pixel resolution of 2 nm. **B)** Sample image with an isotropic Gaussian illumination applied to simulate a finite beam size. **C)** Fourier Transform of B) with log-scale color bar for better visibility. **D)** Zoomed-in image of the red contoured area in C) with visible speckles.

To start, a 2D image of a suspended nanoparticle can be mimicked using circular particles (represented by '1's) on a zero matrix of dimension N_{dim} with a pixel resolution of 2 nm (see Fig. 3.3). To observe speckles, we then added more identical particles into our simulation. Using `numpy.random.randint`, we can generate the

positions of the center pixels of our particles and have the simulation fill in the surrounding pixels to create a grid of randomly oriented pixilated circles. In order to assure no overlap between the particles, a mask was implemented to remove any possible center pixels that would result in a circle that overlapped with any already generated circles. In our simulation, we used a 4096×4096 sample image consisting of 1500 25 nm particles, displayed in Figure 3.4A.

Assuming a Gaussian profile for the transverse amplitude envelope of an incident XFEL beam, a Gaussian “illumination” in the form of a Gaussian kernel can be applied to the sample matrix (Fig. 3.4B) to simulate the experimental condition of varying an XFEL’s beam width. The 2D Gaussian kernel is a convolution of two identical 1D Gaussian arrays. It follows that the standard deviation for the 2D Gaussian is dependent on the 1D Gaussian as follows [33]:

$$\sigma_{2D} = \sqrt{2} \sigma_{1D} . \quad (3.2)$$

We characterise the physical radius of the simulated beam to be the Full Width Half Maximum (FWHM) of our 2D gaussian kernel:

$$w = 2\sqrt{2 \ln 2} \sigma_{2D} \times (2 \times 10^{-9} \text{ m}), \quad (3.3)$$

where $2 \times 10^{-9} \text{ m}$ is our detector pixel size. Figure 3.5 illustrates a contour of what we consider the “beam size” in the case of a Gaussian beam profile, using Eq.(3.3) above.

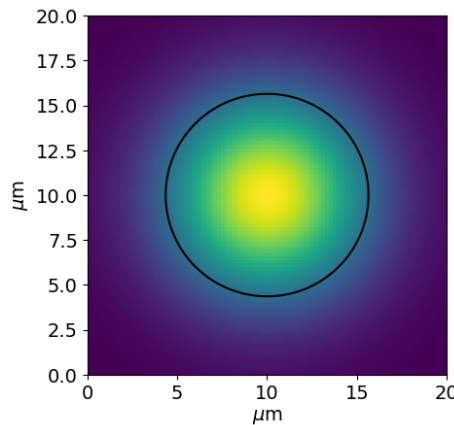


Figure 3.5: Contour (black solid line) of characterised beam size for a Gaussian kernel of $\sigma_{2D} = 282$ pixels ($1.3 \mu\text{m}$) on a 1400×1400 matrix.

A scattering pattern can be obtained by summing up all individual electromagnetic wavelets (which is every non-zero valued pixel) described with the mathematical

equation: $E(x) = A(\cos(kx - \omega t) - i \sin(kx - \omega t))$. A is the amplitude of the wave, which is measured experimentally as the pixel intensity and depends on the distance traveled, x and time, t to the detector. For large matrices, as is the case for our generated sample, this task becomes incredibly time-consuming to run without advanced optimization of the simulation code. Alternatively, knowing that the scattering pattern is an FT of the spatial distribution of scatterers, we can use the Fast Fourier Transform (FFT) function: `scipy.fft.fft2` to obtain the scattering image. The function takes the FT of a 2-dimensional array and returns an array with the corresponding complex coefficients [34]. From Eq.(2.11), we know that taking the square of the absolute value of the complex coefficients will return the intensity. Plotting the image on a log scale (Fig. 3.4C) highlights the scattering pattern from the sample while zooming in (Fig. 3.4D) allows one to clearly observe the speckle interference.

To accurately represent the momentum space axis in our simulated images and plots, the Q-range was determined through understanding that the smallest unit of resolution in real space, the detector pixel size d , is related to the largest value in reciprocal space Q_{\max} via $d = 2\pi/Q_{\max}$. The momentum transfer is centered at the origin of our image, so Q ranges from $[-\pi/d, \pi/d]$. When plotting in Q for data analysis, one then uses `np.linspace(0, π/d , t)` with step size t equal to the dimensions of the dependent variable.

3.3 Form factor fitting

The scattering pattern is recorded on the 2D detector AGIPD. Performing an Azimuthal Integration by which the intensities around the circumference of a circle are defined by a radius Q and centered at the middle of the scattering pattern, we can translate the 2D image into a 1D function that describes the distribution of scattered photons as a function of momentum space. Computationally, a circular mask of the 2D scattering pattern matrix is created where the intensity of all the pixels that fall within the masked area is averaged. The resolution of the azimuthal integration depends on the thickness of the circular mask, which has a minimum threshold of $\sqrt{2}d$ where d is the detector pixel size. Experimentally, the `AzimuthalIntegrator` function in the ‘EXtra-geom’ EuXFEL Python library performs the azimuthal integration automatically for data taken and stored on the Maxwell server.

Up until now, the scattering intensity has mainly been defined as the square modulus of the scattering form factor. Since photons are the source of information in these

experiments, the scattering intensity can also be defined as the differential scattering cross-section, which is the number of scattered photons per unit time at momentum transfer, Q , relative to the incident flux of photons and has units of area per solid angle [4]. It is mathematically described as:

$$\frac{d\sigma(Q)}{d\Omega} = I(Q) = N_p \times (\Delta\rho)^2 \times V_p^2(R) \times |F_p(Q, R)|^2, \quad (3.4)$$

where N_p is the number of particles, $\Delta\rho$ the scattering contrast, V_p the particle volume and $F_p(Q, R)$ is the particle form factor that depends on Q and the particle radius, R [35]. For a monodisperse colloidal sample of silica (SiO_2) spheres, the form factor is governed by the Bessel function:

$$\begin{aligned} |F_p(Q, R)|^2 &= \left(\frac{A(Q, R)}{V(R)} \right)^2 = \left(\frac{4\pi \int_0^R \frac{\sin(QR)}{QR} r^2 dr}{\frac{4}{3}\pi R^3} \right)^2 \\ &= \left(3 \frac{\sin(QR) - QR \cos(QR)}{(QR)^3} \right)^2, \end{aligned} \quad (3.5)$$

where $A(Q, R)$ is the radial integration of the zeroth order of the spherical Bessel function [36] for a sphere particle.

In the case that the silica spheres are not perfectly monodisperse, we can substitute the Bessel function in Eq.(3.4) to include the influence of size polydispersity in the sample. Larger spheres will contribute more scattering than small ones which can be represented with the Schulz(-Zimm) distribution function [37]:

$$n(R) = \frac{[(z+1)/R_0]^{(z+1)} R^z}{\Gamma(z+1)} \exp - \left[\frac{(z+1)}{R_0} \right] R, \quad (3.6)$$

where z is the integer parameter that describes the width of the distribution, and R_0 is the average particle size. Figure 3.6 illustrates how the z parameter in the Schulz distribution changes the weight of polydispersity as well as how it differs from a Gaussian distribution for high z .

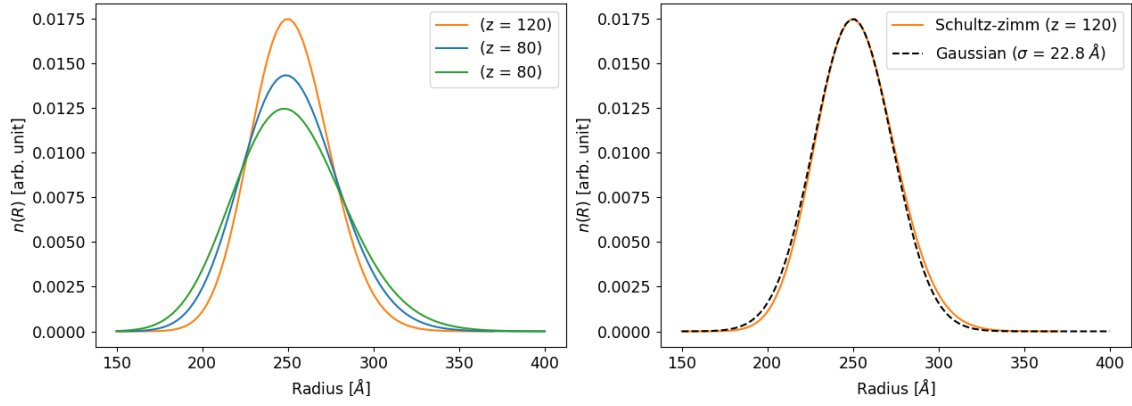


Figure 3.6: *Left:* The Schulz distribution $n(R)$ for various values of z . *Right:* The Schulz distribution with $z = 120$ (orange solid line) plotted next to a Gaussian distribution (dashed line) of equal mean radius R_0 .

The scattering intensity is then given by integrating the monodisperse form factor over Eq.(3.6):

$$I(Q) = N(\Delta\rho)^2 \int_0^\infty V_P(R)^2 \left[3 \frac{\sin(QR) - QR \cos(QR)}{(QR)^3} \right]^2 n(R) dR. \quad (3.7)$$

Eq.(3.7) above was solved in Aragón and Pecora's 1976 article on Dynamic Light Scattering (DLS) for the Schulz distribution [37] and implemented as functions in Python for modeling polydispersity.

3.4 Autocorrelation Function

To characterise the spatial variation and homogeneity of an image, it can be useful to study the correlation of the image with itself - also known as an autocorrelation. To study the spatial structure of speckles, we can investigate the degree of correlation a speckled image has against itself for varying spatial separations $\Delta x = x_1 - x_2$ and $\Delta y = y_1 - y_2$ for positions (x_1, y_1) and (x_2, y_2) on the detector plane. The autocorrelation function Γ_I describes how rapidly the distribution of scatterers varies from point to point. Intuitively, we expect total correlation for two images that have no spatial separation ($\Delta x = \Delta y = 0$), and for the correlation to fall to zero with an increase in spatial separation [38]. The rate at which the function falls to zero reveals to us the degree of correlation, which is related to the size of the speckles.

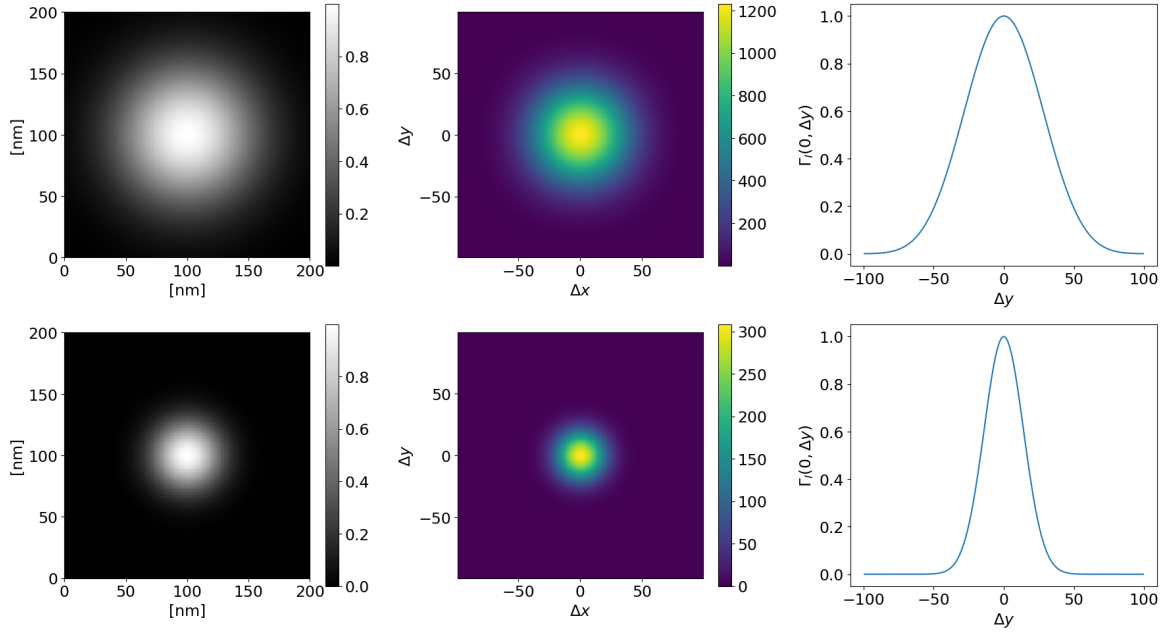


Figure 3.7: Demonstration of the 2D autocorrelation, $\Gamma_I(\Delta x, \Delta y)$, of two Gaussian kernels along with a horizontal 1D slice of the autocorrelation. *Left:* 2D Gaussian kernels representing two different spot sizes with a color bar displaying the intensity. *Middle:* 2D autocorrelation, $\Gamma_I(\Delta x, \Delta y)$, of the images on the left. *Right:* y -cut of $\Gamma_I(\Delta x, \Delta y)$ for $\Delta x = 0$.

In his book, Goodman [8] used a complex correlation coefficient to describe the degree of correlation between two values of the same variable at a spatial offset of $(\Delta x, \Delta y)$:

$$\mu(\Delta x, \Delta y) = \Gamma_A(\Delta x, \Delta y) / \Gamma_A(0, 0) \quad (3.8)$$

where $\mu(0, 0) = 1$. The square modulus of the complex correlation coefficient is used to obtain the normalised intensity autocorrelation function:

$$\Gamma_I(\Delta x, \Delta y) = 1 + |\mu(\Delta x, \Delta y)|^2 \quad (3.9)$$

Since we are interested in the speckles present in the scattered image and not the enveloping scattering pattern describing the form factor, we zoom in on a Region Of Interest (ROI) centered at a specific Q value. For our analysis, we chose an ROI with high speckle intensity (64×64 pixels) centered at $Q = 0.01 \text{ \AA}^{-1}$.

$\Gamma_I(\Delta x, \Delta y)$ was computed using `scipy.signal.correlate2d`, which works well for large arrays. After obtaining the 2D-autocorrelation function, a vertical ($\Delta x = 0$) or horizontal ($\Delta y = 0$) slice through the origin of the autocorrelation function was taken

to analyse the central peak feature. Figure 3.7 demonstrates the autocorrelation of two different images, where the central peak is featured in the 1D plots of the horizontal slice. At $\Delta x = \Delta y = 0$, Eq. (3.9) takes the maximum value of 1, and we expect larger speckle features to exhibit broader central peaks. The Full Width Half Maximum (FWHM) of the correlation peak is considered a reasonable measurement to characterise the speckle size [38]. Since the width of the autocorrelation function is $\sqrt{2}$ larger than the speckle size of the individual image due to the convolving nature of the operation. In the Gaussian approximation, $\text{FWHM}/\sqrt{2}$ is then a good estimate of the speckle size, S .

4.1 Speckle simulator and SAXS analysis

For our 4096×4096 sample matrix of 1500 randomly generated 25 nm circular particles, we are able to successfully simulate the occurrence of a speckle pattern. For a Gaussian beam of $w = 4 \mu\text{m}$, zooming in on an ROI in the Q range $[0.007, 0.014] \text{ \AA}^{-1}$ provides a good inspection of the speckles. Figure 4.1 compares this with an ROI in a similar Q range for the experimental data of 25 nm LUDOX[®] at 9.0 keV. The speckles from the experimental data are much smaller than that of the simulation, which suggests the experimental beam size was larger than $4 \mu\text{m}$.

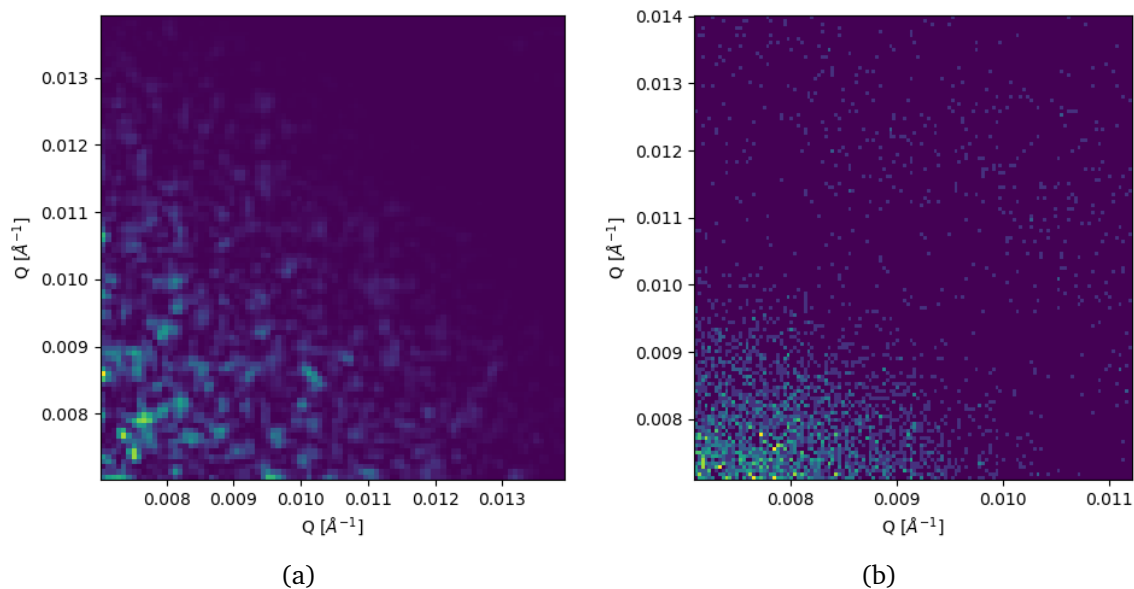


Figure 4.1: a) Simulated speckle pattern ROI for a Gaussian beam of $w = 4 \mu\text{m}$ centered around $Q = 0.01 \text{ \AA}^{-1}$. b) Experimental single shot image ROI for $E = 9.0 \text{ keV}$ centered around $Q = 0.01 \text{ \AA}^{-1}$.

An example of a simulated SAXS pattern is displayed in Figure 4.2 and shows the well-expected concentric circles for scattering from spherical objects. The first four dark fringes from the center of the pattern have a smooth circular profile, but this begins to break down at larger Q . This is expected as the squiggly profile of the dark fringes toward the edges of the pattern reflects the pixilated nature of the circles (see Fig. 3.3) in our matrix image of the sample. At high Q , short distances are probed in

real space, which would result in the expression of the jagged nature of the particle shapes when zoomed in.

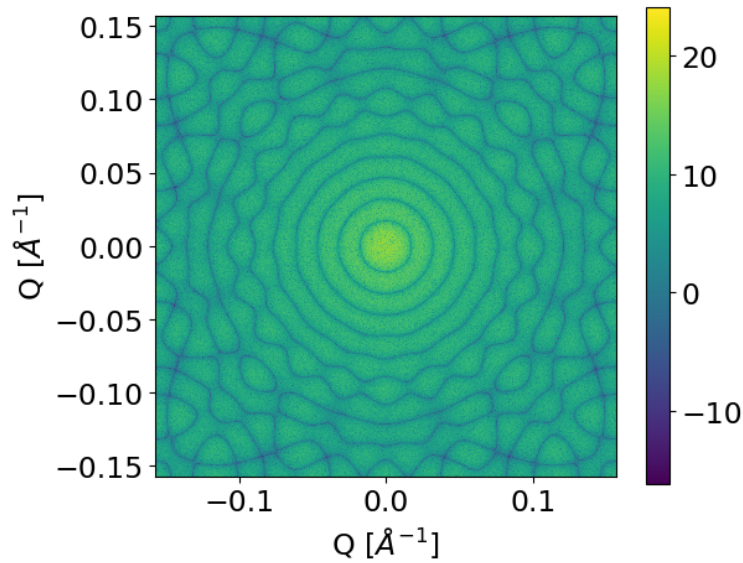


Figure 4.2: Fourier transform of a Gaussian illuminated matrix sample to simulate the SAXS pattern of 25 nm circular particles with a log-scale colorbar.

4.1.1 Scattering pattern

Performing an azimuthal integration of the scattering pattern, we can analyse the validity of our simulation by comparing the computer-generated curve with the theoretical form factor of monodispersed hard-spheres (Eq.(3.5)). The two curves are plotted together in Figure 4.3, where they exhibit a large degree of similarity up until just after the first dark fringe. Past that point, it can be noted that the simulated scattering curve has a stretched period of oscillation as well as some dampening. Selecting a radius parameter of 258 Å for the model returned the best visual results for the fit of our simulated data, which coincided well with the nature of our generated sample, which consisted of 25 nm circles.

The dampening of the fringes at high Q is attributed to the squiggly dark fringes that can be observed towards the outer corners in Figure 4.2. When performing the radial averaging at high Q , the intensities had larger fluctuation along the circular mask, causing the contrast between dark and bright fringes to decrease.

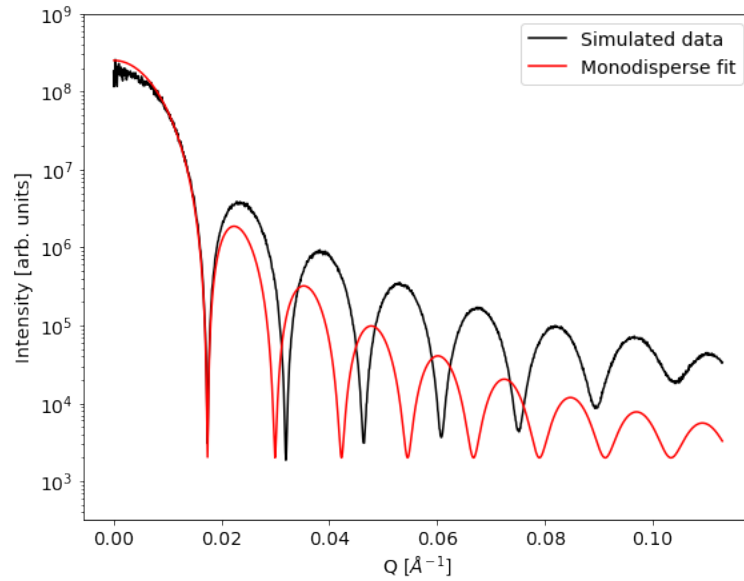


Figure 4.3: Comparison of simulated SAXS pattern with the monodisperse fit (hard-sphere form factor). The result from the simulated scattering curve of a 2D matrix image of spherical 25 nm nanoparticles (black line) is superimposed with the theoretical monodisperse hard-sphere form factor (red line).

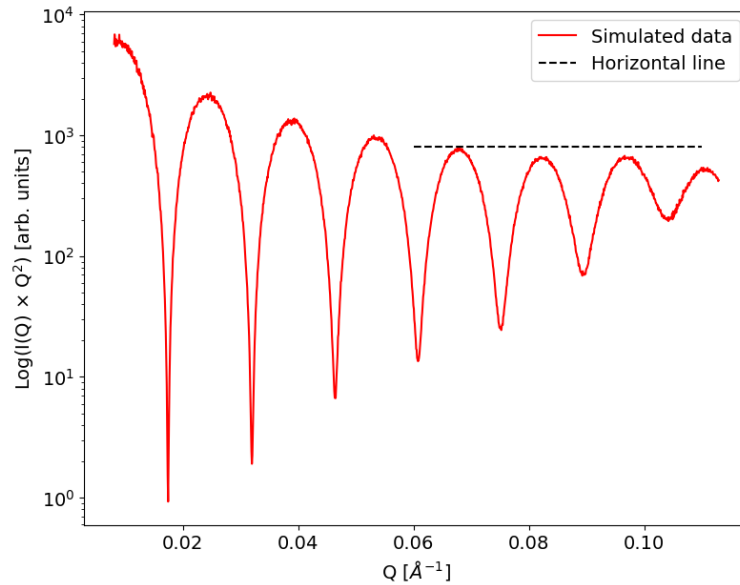


Figure 4.4: Simulated scattering intensity data multiplied by Q^2 as a function of Q . The dashed horizontal line is used as a guide for the eye to show $I(Q) \propto Q^2$ for $Q > 0.06 \text{ \AA}^{-1}$.

Form factors are highly dependent on the dimensionality of the particle due to the integral element in Eq.(2.12). The broadening observed in our simulated data is most likely due to the 2D nature of our simulation, while Eq.(3.5) is used to describe 3D scattering. This can be examined by performing a Porod analysis. For a sphere, the element of integration is the unit volume, $dV = 4\pi r^2 dr$, where r is the particle

radius. From this, we can tell that the form factor will evolve with r^2 . For a 2D disk, the element of integration is the area $dA = 2\pi r dr$, and the form factor evolves with r [4]. Recalling that $I(Q) \propto |F(Q)|^2$ and $r \propto 1/q$, we can conclude that while $I(Q) \propto 1/Q^4$ in the Porod regime for 3D spheres, we should expect $I(Q) \propto 1/Q^2$ for our 2D matrix of circles. Figure (4.4) below is the same simulated scattering curve plotted as a product of Q^2 . The horizontal slope at high Q suggests a $I(Q) \propto 1/Q^2$ which supports the proficiency of our simulation.

4.1.2 Experimental SAXS Analysis

The scattering images obtained from LUDOX[®] were averaged over 500 pulses for $E = 9$ keV to acquire better statistics and remove the speckles for a consequently smoother curve. Figure 4.5 is an example of a SAXS pattern averaged over multiple shots taken at MID for our sample. In the averaged image, the scattering pattern of the spherical nanoparticles is made clearly visible with a log-scale color bar to make low-intensity outer rings more prominent. A dark detector image is taken at the beginning of the experiment to use in the data correction pipeline, mainly to remove any background and detector noise. Occasionally, the AGIPD will have temporary hot pixels with bright intensities that are unrelated to the scattered photons (exhibited on the right side of the bottom module in the upper right quadrant in Fig. 4.5). To correct this, a rectangular mask the size of the area with dysfunctional pixels is used to remove the erroneous intensities from our data.

The image was then radially integrated using the pyFAI library and unfolded over the entire Q -range to obtain the scattering cross-section plot displayed in Figure 4.6. Up until the fourth oscillation, the scattering curve exhibits a smooth trend with noise prominence starting around 0.04 \AA^{-1} .

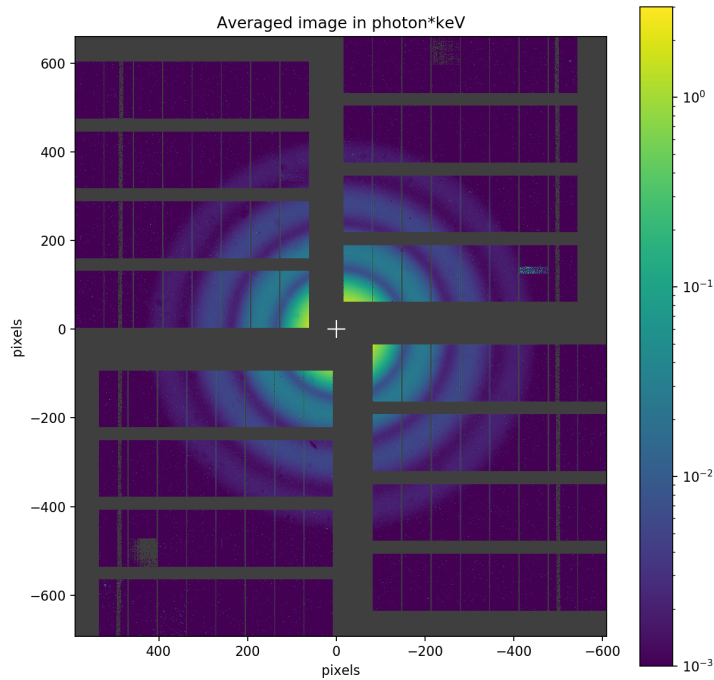


Figure 4.5: Experimental SAXS pattern of 25 nm LUDOX[®] taken with an energy of 9 keV, averaged over 500 single shot AGIPD images (color bar in log-scale) at the MID station the European XFEL.

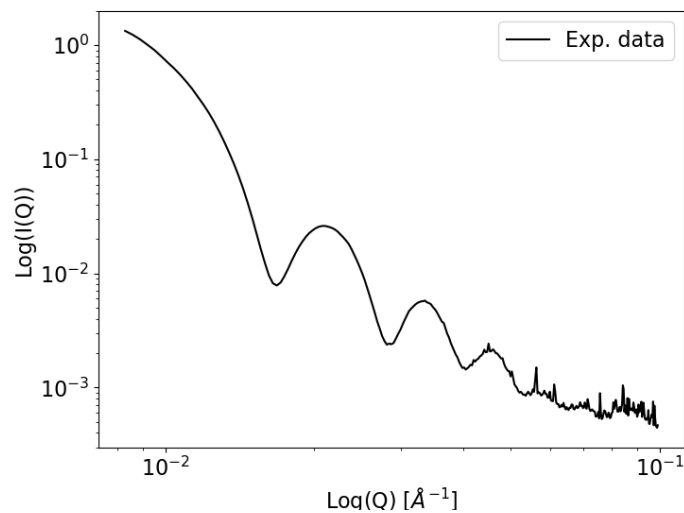


Figure 4.6: Scattering intensity $I(Q)$ of 25 nm LUDOX[®] taken with an XFEL beam ($E = 9$ keV), averaged over 500 single shot images.

4.1.3 Porod Analysis

A Porod analysis of the SAXS curve can be performed to investigate whether the data at high Q contain any background intensity unrelated to the elastic scattering. At high Q , the intensity is proportional to the surface area of the sphere [4], which

means $I(Q) \propto Q^{-4}$. To check this, the intensity was plotted as a product of Q^4 , which for $I(Q) \propto Q^{-4}$ means the slope will be flat.

Figure 4.7 shows $I(Q) \times Q^4$ versus Q in log-log plots. In Fig. 4.7a, the intensity has a flat gradient up until $Q \approx 0.05 \text{ \AA}^{-1}$. The intensities above the dashed line are contributions from background and inelastic scattering. This can easily be removed from our data by simply subtracting a constant, $I = 10^{-3}$, from $I(Q)$. Fig. 4.7b shows the scattering curve after correction. After subtraction, we chose to focus our data analysis and fitting in the Q range up to 0.05 \AA^{-1} .

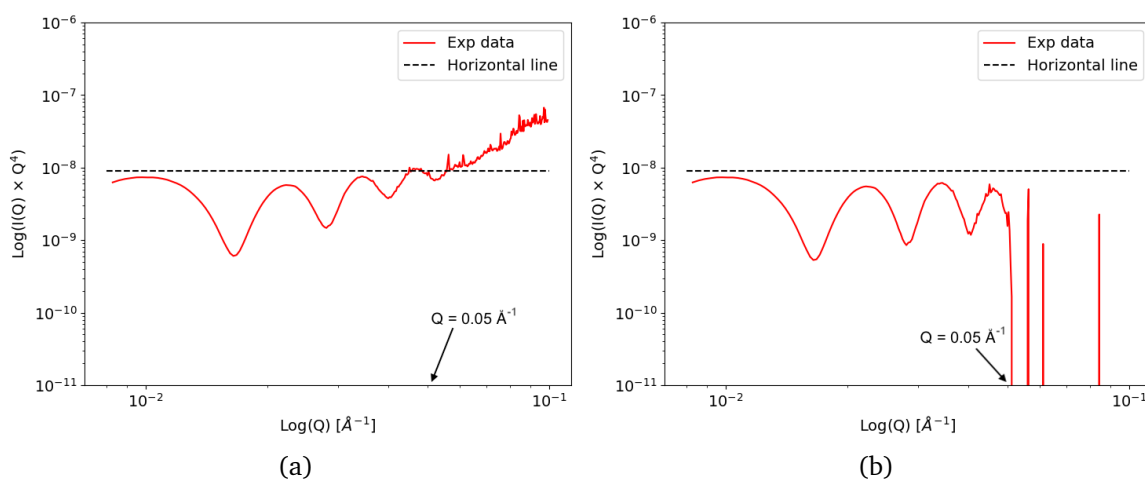


Figure 4.7: Porod analysis of the radially integrated scattering intensity data multiplied by Q^4 for 25 nm LUDOX[®]. A horizontal dashed line is used for visual reference. (a) Scattering pattern before subtracting a constant background intensity. (b) Scattering pattern after subtracting a constant of 10^{-3} . Arrows indicate the maximum Q value included in our statistical fitting.

4.1.4 Form Factor fitting

Fitting the corrected data with the monodisperse form factor described in Eq.(3.5), we were able to get the result displayed in Fig.4.8 with a dashed line. Upon inspection, it was clear that there was some smoothing to the experimental data that the monodisperse hard-sphere form factor does not take into account. In experimental results, there is often data smearing due to elements such as beam bandwidth, $\Delta\lambda$, or the finite resolution of a detector.

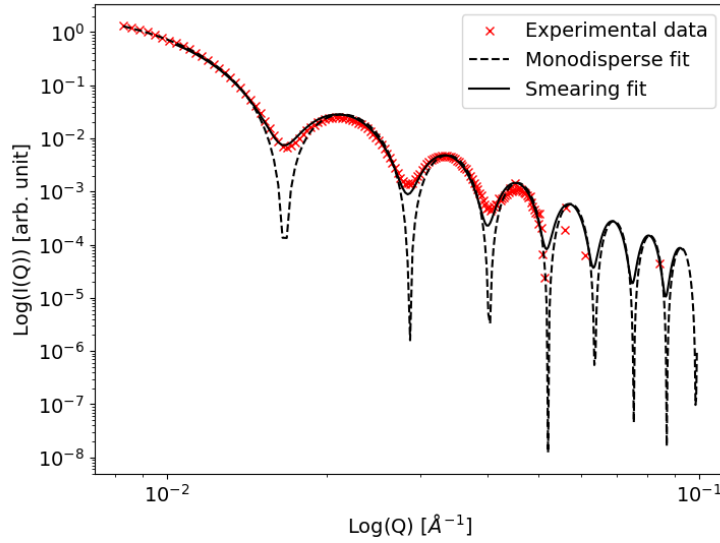


Figure 4.8: Experimental scattering intensity of 25 nm LUDOX[®] acquired at European XFEL fitted with the spherical monodispersed model (dashed line) with parameters: $R = 271 \text{ \AA}$, scale = 4.7×10^{-8} . Applying the Q-resolution smearing to the same model provided an alternative fit (solid line) with a Q-resolution smearing ranging from [2 - 12] %.

AGIPD has a finite resolution that depends on the size of the pixel ($200 \mu\text{m} \times 200 \mu\text{m}$) as well as the distance of the detector from the sample (7.9 m). To apply instrument smearing to our scattering cross-section equations, we can convolve the monodisperse model with a Gaussian function that had a sigma depending on the smallest resolvable solid angle subtended by one pixel. The Q resolution was found by differentiating Bragg's law (Eq.2.9) with respect to the scattering angle:

$$\frac{dQ}{d(2\theta)} = \frac{2\pi}{\lambda} \cos\left(\frac{2\theta}{2}\right) \quad (4.1)$$

$$\Rightarrow dQ = \frac{2\pi}{\lambda} \cos\left(\frac{2\theta}{2}\right) d(2\theta), \quad (4.2)$$

where $d(2\theta) \approx \frac{\text{AGIPD pixel resolution}}{\text{sample-detector distance}} \approx 0.0015^\circ$ using the small angle approximation. Dividing $d(2\theta)$ by $2\sqrt{2} \ln 2$ is a reasonable approach to characterising the resolution smearing. This way, the standard deviation of the Gaussian allows us to take into consideration systematic errors like charge sharing between neighboring pixels. When performing the fit, this magnitude of smearing created over-dampened oscillations, so we multiplied dQ by 0.43 to obtain the correct level of smearing. This resulted in a dQ/Q with a range of [2 - 12]%. The results of the smeared fit were visibly an improvement from the simple monodisperse model (see solid black line in Fig. 4.8), however, deviations around the local minima still exist for the second and third dark fringes.

We then also decided to fit using a polydisperse model in the case that the spherical particles are not identical in size. Using the Schulz distribution to model for polydispersity, we were able to get the following results displayed in Fig. 4.9 using the evaluated version of Eq.(3.7) given in Aragon and Pecora's article [37].

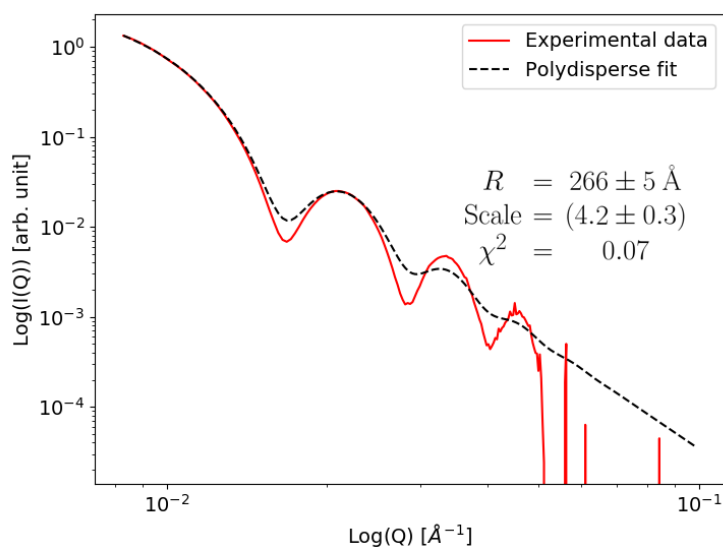


Figure 4.9: The fitted curve of experimental scattering intensity of 25 nm LUDOX[®] acquired at European XFEL using the polydisperse spherical shell model ($R = 266 \text{ \AA}$, $z = 120$, scale = 4.2).

For a mean radius of 263 \AA and a polydispersity size distribution of $z = 120$, the fit in black dashed lines was visibly more smooth than our experimental data, which suggests a Schulz distribution with $z = 120$ is too high a degree of polydispersity.

In Python, factorials of numbers greater than 120 become computationally challenging in our defined function. We then turned to Sasview, a black box SAXS curve fitting software, to obtain the optimal values for particle radius, R . The data was

imported to SasView and evaluated with four different variations of the hard sphere model: monodisperse, monodisperse with instrument smearing, polydisperse, and polydisperse with instrument smearing. The polydispersity model in SasView had a Gaussian distribution for R . The degree of polydispersity, PD , was defined as [39]:

$$PD : \sigma/\bar{R}, \quad (4.3)$$

where σ is the standard deviation of the normal distribution, and \bar{R} the mean radius. The polydisperse hard sphere model with instrument smearing is displayed in Figure 4.10, and the three other models and their plots can be found in the Appendix in Section 7.5.

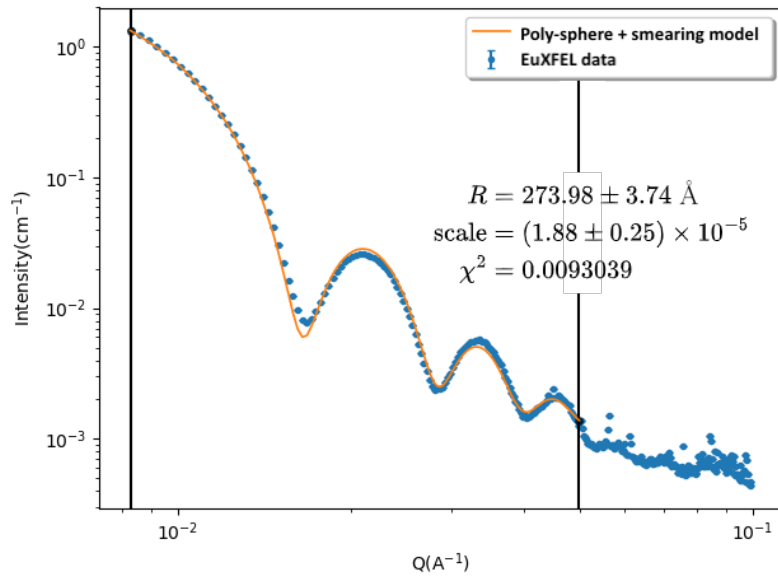


Figure 4.10: Sasview fitting of the scattering intensity of 25 nm LUDOX[®] acquired at the European XFEL with a Gaussian polydisperse hard sphere model (PD : 0.03 ± 0.03) Å including $dQ/Q = 5\%$ instrument resolution smearing.

The fitted parameters for each Python and SasView model are presented in Table 4.1 below along with weighted χ^2 values. With intensity plotted in log-scale, the residuals calculated at high Q will not have the same impact as residuals at low Q . This is due to the intensity ranging across three orders of magnitude for our recorded scattering angles. To correct for this, a *weight* factor is introduced to the χ^2 equation [40]:

$$\chi^2 = \sum_i (Y_i - theory_i)^2 / weight_i^2 \quad (4.4)$$

$$= \sum_i (Y_i - theory_i)^2 / Y_i. \quad (4.5)$$

In the case of our goodness of fit, we normalised the residual by weighting it with the square root of the observed intensity. For a good fit, χ^2 tends to 0. The fitting performed in Python does not include optimisation of fitting parameter errors. We assumed parameter uncertainties for the Python fits based on the condition that the χ^2 is doubled from its minimum value for each of the parameter's error limits.

Table 4.1: Fitting parameters for LUDOX[®] SAXS data for variations of the hard-sphere model. The distribution of polydispersity is Schulz for Python (Eq.(3.6)) and Gaussian for Sasview.

	Model variations	Radius R [Å]	Scale* [$\times 10^{-5}$]	χ^2
Python	Monodisperse	271 ± 6	$(4.7 \pm 0.3) \times 10^{-3}$	0.08
	Monodisperse + smear**	268 ± 10	$(1.5 \pm 0.3) \times 10^{-6}$	0.01
	Polydisperse ($z = 120$)	266 ± 5	$(4.2 \pm 0.3) \times 10^5$	0.07
Sasview (hard sphere model)	Monodisperse	272 ± 3	1.7 ± 0.2	0.05
	Monodisperse + smear***	274 ± 3	1.9 ± 0.2	0.01
	Polydisperse (0.075 ± 1.15)	270 ± 4	1.9 ± 0.3	0.009
	Polydisperse + smear*** (0.03453 ± 2.336)	274 ± 4	1.9 ± 0.3	0.009

*The scale parameter includes the electron density contrast $\Delta\rho$ as well as V_p .

** $dQ/Q = (2 - 12)\%$.

*** $dQ/Q = 5\%$.

Out of the three Python fits performed, the monodisperse model with instrument smearing resulted in the best goodness-of-fit ($\chi^2 = 0.01$). This result coincides

with the results obtained for a monodisperse fit with similar instrument smearing evaluated in SasView. The fit with the best goodness-of-fit in Sasview turned out to be the two Gaussian distributed polydisperse hard sphere models (χ^2 of 0.009 each).

When applying instrument smearing, the accuracy with which one can match the theoretical model and experimental data decreases, and we would expect this to reflect in the errors of the recovered parameters. In both the monodisperse and polydisperse models, applying instrument smearing increased the uncertainty in radius by 0.62 Å and 0.02 Å respectively. For the monodisperse model, applying a 5% instrument smearing improved the χ^2 value of the fit, while it had no effect on a polydisperse model's χ^2 . In fact, the inclusion of instrument smearing for the polydisperse fits was able to reduce the degree of polydispersity estimated, however, this is compensated by an increase in average radius by 4 Å compared to a model without smearing.

The scaling factor of each model, which includes parameters such as the density contrast and particle volume (for monodisperse models), all fall within the same range when taking into account the error limits. While our own monodisperse model with instrument smearing recovered a radius range closest to 25 nm, the recovered radius from the SAXS fits are all larger in dimension than expected. This could be due to the simplicity of our model not including other parameters such as smearing due to the XFEL radiation bandwidth $\Delta\lambda/\lambda$, even though dQ/Q from radiation bandwidth is negligible compared to resolution smearing.

Overall, with a notable increase in goodness-of-fit from monodisperse to monodisperse with smearing seen in Table 4.1, we can conclude that while there could be a degree of polydispersity in our sample, the larger contributing factor to the dampened oscillations is the Q-resolution smearing from instrument limitations.

4.2 Speckle Analysis

First taking a look at the speckles from our simulated SAXS patterns, 40 beam sizes ranging from 2.33 μm to 6 μm were simulated and applied to the sample to show a trend in the evolution of speckle sizes with changing beam size. An ROI centered around $Q = 0.01 \text{ \AA}^{-1}$ (Fig. 4.1) in each FT image was then selected for performing the autocorrelation. Computing the autocorrelation returns a 2D matrix with the corresponding correlation coefficients for each spatial delay Δx or Δy (in units of pixel, which can be converted to units of Å^{-1}). By taking a 1D slice of the matrix

down the middle column, we make a one-dimensional y -cut of the autocorrelation to investigate. Note the central peak feature over a large pedestal background in the right image in Fig. 4.11.

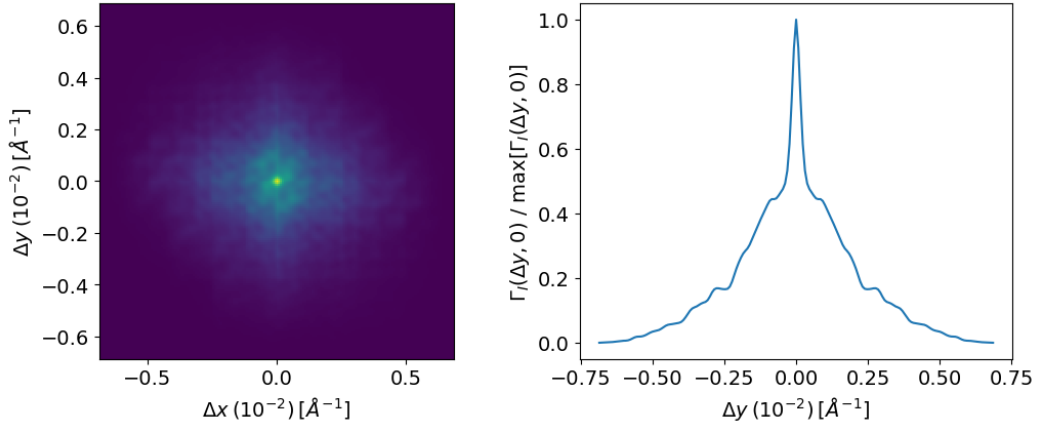


Figure 4.11: *Left:* 2D spatial autocorrelation of the ROI of a simulated speckle pattern for 25 nm sphere particles with beam size $w = 1.7 \mu\text{m}$. *Right:* Normalised central y -cut of the 2D-autocorrelation of the simulated speckle pattern.

For the simulated data, the 1D autocorrelation function for various beam sizes all exhibit the same pedestal feature which arises from the average background intensity provided by the structure of the sample. We can remove this background by fitting it with a Gaussian and subtracting it from $\Gamma_I(\Delta y, 0)$. Figure 4.12 below shows $\Gamma_I(\Delta y, 0)$ after background subtraction as well as a zoomed-in plot to better show the variation in peak widths for different Gaussian beam illuminations.

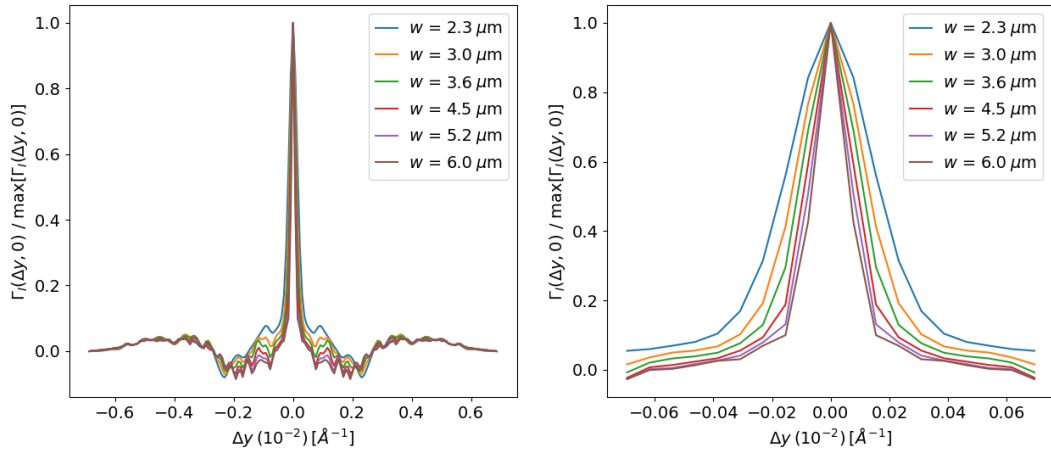


Figure 4.12: *Left:* Background subtracted y -cut of the 2D-autocorrelation of the simulated speckle pattern for various Gaussian beam sizes w . *Right:* Zoomed in plot of central peak feature in the left plot

In the experimental data set, $\langle \Gamma_I \rangle$ represents the averaged y -cut autocorrelation function for 18 consecutive single-shot images. Since speckle patterns are independent of

the spatial position of scatterers, averaging over multiple $\Gamma_I(\Delta y, 0)$ will still display the speckle features. On the other hand, $\Gamma_{\langle I \rangle}$ represents the y -cut autocorrelation function for an averaged image of the scatter pattern, so the correlated function only carries the signature of a time-averaged structure factor. $\langle \Gamma_I \rangle - \Gamma_{\langle I \rangle}$ results in a $\Gamma_I(\Delta_{x,y}, 0)$ function where the background is removed (shown in Fig. 4.13).

After subtraction, we are left with just the central peak, which is related to the size of the speckles. To characterise the central peak, we can fit a Gaussian to the zoomed-in plot of the central peak (to remove any influence from the wings of the function) and extract the standard deviation σ to find the FWHM using:

$$\text{FWHM} = 2\sqrt{2 \ln 2} \sigma \approx 2.355\sigma .$$

The results of each individual fit of the background subtracted Γ_I peaks for the simulation can be found in Section 4.2.2 in the appendix. The experimental Γ_I peaks are fitted and the speckle width, S , is characterised as $\text{FWHM}/\sqrt{2}$.

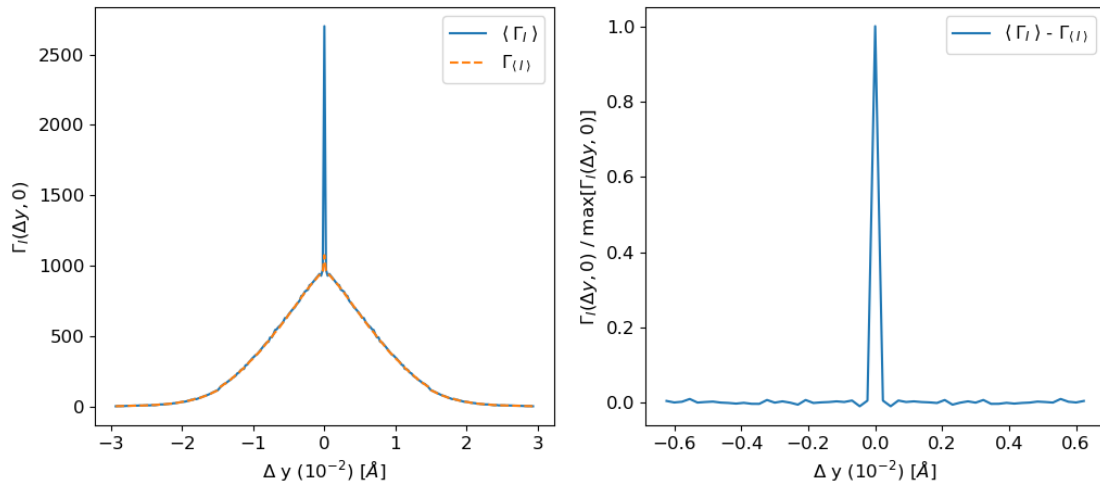


Figure 4.13: y -cut of autocorrelation function of experimental ROI for 25 nm LUDOX[®]. *Left:* Blue solid line for $\langle \Gamma_I \rangle$. Orange dashed line for $\Gamma_{\langle I \rangle}$. *Right:* Normalised autocorrelation function with average intensity subtracted.

4.2.1 LUDOX[®] experiment (ΔE)

The goal of the LUDOX[®] experiment was to vary the energy and investigate whether the speckle size is truly inversely proportional to the beam size or not. The results for an energy range of (8.7 - 9.2) keV showed speckles that were significantly smaller in resolution compared to the speckles resolvable in our simulation (visible in Fig. 4.1). This translated into a central peak feature that had a sharp delta-like profile upon performing the autocorrelation of the ROI. This was a feature that arose as a

consequence of the FWHM of the peak residing on the same order of magnitude as one pixel. In the case of our simulated data (where our detector resolution is 10^4 times higher), large speckles translate to a central peak feature in Γ_I that is more Gaussian in profile, which is also easier to fit using `scipy.optimize.curve_fit`.

From inspection, the broad pedestal intensity was removed with better accuracy for the experimental data (Compare Fig. 4.12 *Left* with Fig. 4.13 *Right*). This is judged based on the lack of fluctuation on either side of the background subtracted autocorrelation function's central peak.

Plotting the extracted speckle widths for both the simulation and the LUDOX[®] experiment, we observe in Figure 4.14 that for both simulated and experimental results the speckle size reduced with increasing beam size. While it was possible to plot the speckle size as a function of beam size in our simulations, the absolute beam size could not be inferred from just the energy of the XFEL beam in the experiment. For the experimental data, speckle size was plotted as a function of energy squared, E^2 . Assuming that the beam size varies linearly with focal length, we can derive the relation between focal length and energy with the theory presented in Sec. 2.1. From Eq.(2.1), (2.2) and (2.3) about the refractive properties of X-rays, it is known that $E \propto \frac{1}{\lambda}$ and $\frac{1}{\lambda^2} \propto \frac{1}{\delta}$. The focal length of a lens is inversely proportional to δ [21], which leads us to $f \propto E^2$.

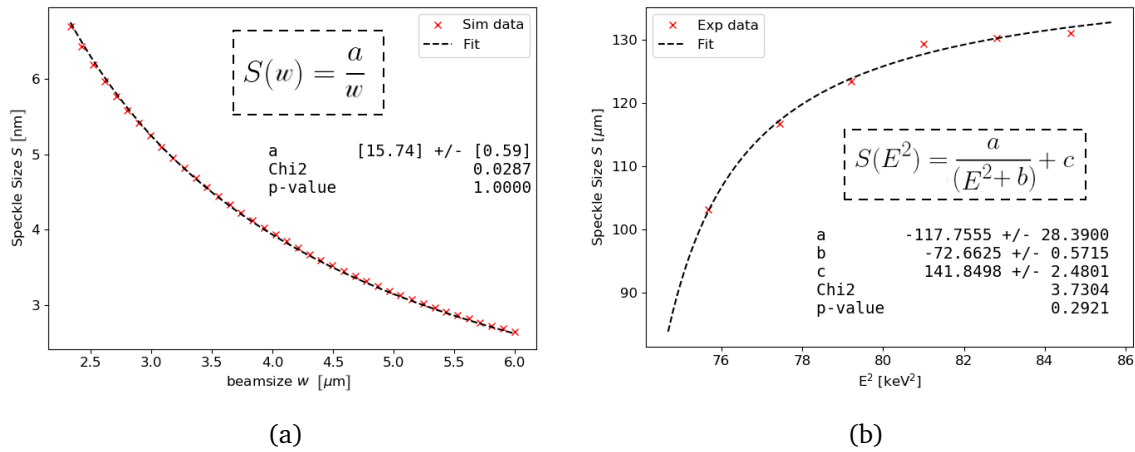


Figure 4.14: Scatter plot of speckle size S as a function of beam width b or energy squared E^2 . The data was fitted with inverse functions and the parameter values are listed. (a) Results obtained from simulation. (b) Results obtained from varying the energy of the beam using 25 nm LUDOX[®].

For the simulated results (Fig. 4.14a) the scaling parameter, a in $f(x) = a/x$ was fitted with Iminuit and found to be 15.74 ± 0.59 . The magnitude of a is not as important as the sign - which tells us whether the focal point is before or after the

sample in our set-up. In the experimental results, $a \approx -117 \pm 28$ has a negative sign. An increase in speckle size due to a larger focal length meant that at E_0 , the focal point of the XFEL beam was before the sample in order for the beam size to decrease with increasing E (see Fig. 3.2).

Plotting $S(E^2)$ and fitting with an inverse function (with scaling parameter a , b and c), we obtained a χ^2 of 3.7304, and with 3 degrees of freedom that corresponded to a p value of 0.2921. With these statistics, we can assume that this result provided evidence of an inverse relation between speckle and beam size. This is expected as large dimensions in real space correspond to small dimensions in reciprocal space.

For a Gaussian beam, we expect the beam size to evolve following Eq.(2.6). The function $w(z)$ is symmetric around $z = 0$, which is also the focal point of the beam. In Figure 4.14 both cases only show one of the solutions. If we increased the energy beyond 9.2 keV, at some point we expect the symmetric profile displayed in Fig. 2.5.

4.2.2 Vycor experiment (NaFo Lens)

A more experimentally efficient way to vary the beam size is to apply a NaFo lens before the sample in the experimental hutch. With the Vycor experiment at MID, we were able to create a scan of how the speckle size changes with varying beam size by moving the NaFo lens up or down the direction of beam propagation. With a greater variation of beam sizes, we expect to fit the evolution of w using Eq.(2.6). A static sample was chosen to produce results with static speckles as the purpose of this experiment was unrelated to scattering dynamics. Figure 4.15 shows a typical SAXS pattern taken at MID of our 10 nm Vycor sample.

The process of analysis is almost identical to that of the LUDOX[®] experiment. There is, however, a limited amount of experimental data for Vycor where only the first 100 pulses of each train were recorded. Each pulseID should correspond to a single-shot image, yet in our set of images, some lacked the sufficient intensity to use for analysis. This could be a result of low intensity due to poor transmission resulting from flux attenuation from the NaFo lens. The XFEL beam's spectral inconsistency could also be a factor. As a result, This meant that our automated data processing script could not be used to its full extent as each ROI had to be inspected by eye before processing. Due to time constraints, this meant that in this thesis only one image was taken for each NaFo lens position to obtain a Γ_I function to fit.

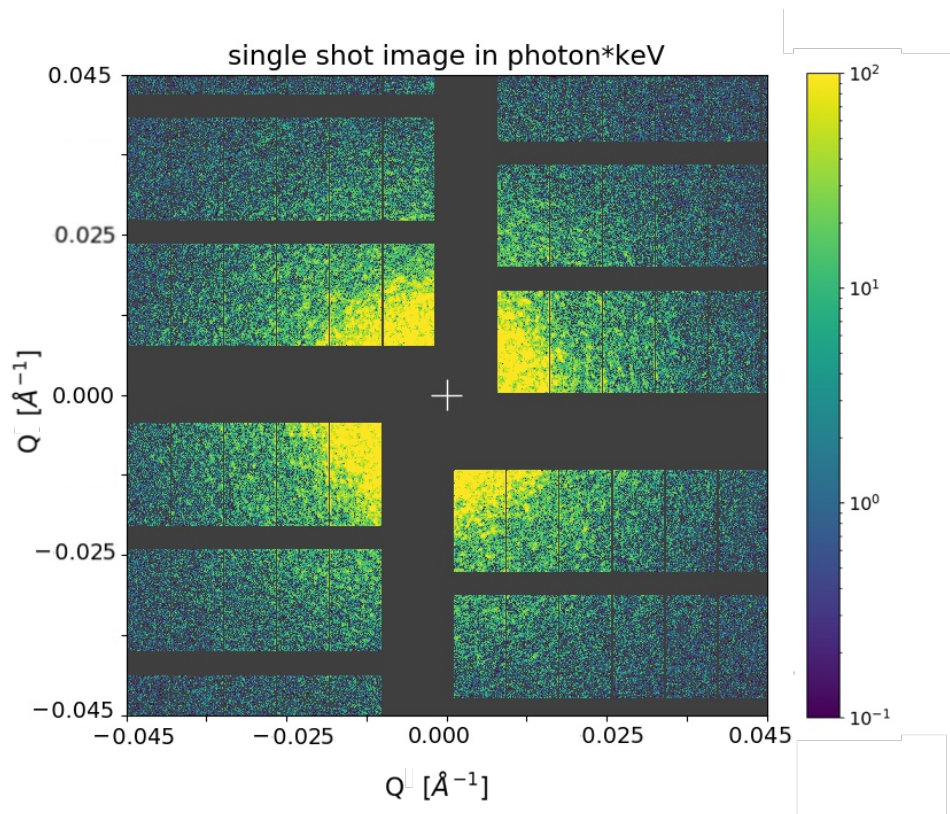


Figure 4.15: Experimental single-shot SAXS pattern of 10 nm Vycor glass taken with a beam energy of 9 keV using the AGIPD (color bar in log-scale) at the MID station at European XFEL.

The autocorrelation was performed with the same procedures as for the LUDOX[®] analysis - where the broad pedestal feature is subtracted with the autocorrelation function $\Gamma_{\langle I \rangle}$ averaged over 500 single-shots (which washes away speckles even for a static sample) for the background intensity features of the SAXS pattern (see Fig.4.16). The computer motors adjusted the lens position at a rate that matched the frequency of train deliveries, which meant that each train represented a different beam size. 30 train IDs were sampled at equally spaced intervals along the range of motor positions (referred to as “lotz” at MID), and the fit results are displayed in Figure 4.17.

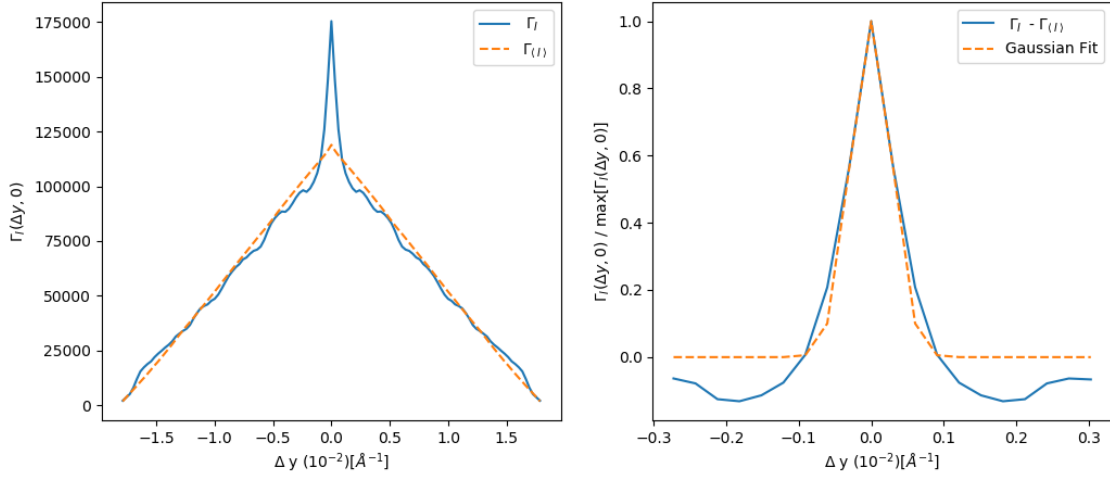


Figure 4.16: y -cut of autocorrelation function of ROI in Vycor experimental data. *Left:* y -cut of Γ_I function of ROI (blue solid line). The orange dashed line represents the background to be subtracted, $\Gamma_{\langle I \rangle}$. *Right:* Normalised autocorrelation function with average intensity subtracted (blue solid line). The orange dashed line is the Gaussian fit for characterising the width of the peak.

The central peak was the most challenging to fit in this experiment. Due to the inconsistency in scattering pattern quality, in order to obtain enough ROIs for an average autocorrelation function, $\langle \Gamma_I \rangle$, a large amount of time would need to be allocated to hand-selecting ROIs for each lens position. Thus multiple ROIs per lens position were not included in this work as a result of time constraints, which meant attaining proper statistics is a priority in any follow-up investigation. Nevertheless, we still present the following results as we believe it shows great promise in our endeavor to characterise speckles and use them in experimental analysis.

The speckle size, S recovered from the Gaussian fits was dependent on the distribution's standard deviation, which was processed in units of pixels. The $\text{FWHM}/\sqrt{2}$ multiplied by the angle subtended by one pixel (≈ 0.00003 rad for AGIPD) is then considered the angular speckle size, S_θ . Using the trigonometric relation between S_θ and the distance of the detector, L , we then determined the width for the speckle on the detector plane with the following calculation:

$$S = S_\theta \times L .$$

Now our speckle size has units of length. We know that the speckle size is indeed inversely proportional to the beam size from our results in Section 4.2.1 and that they also depend on the wavelength of the FEL beam. Thus, we can consider the following equation for relating the speckle size to the beam size:

$$S = \frac{\lambda L}{w} \iff w = \frac{\lambda L}{S}. \quad (4.6)$$

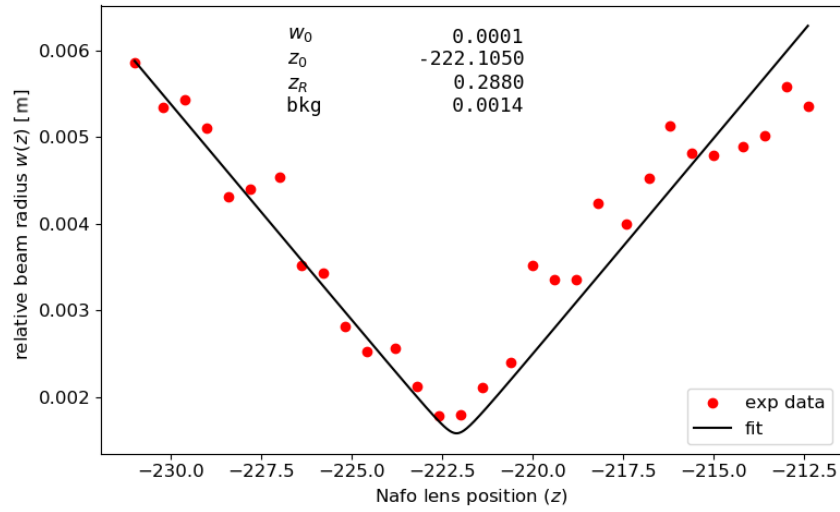


Figure 4.17: Preliminary plot showing the evolution of beam width as a function of lens position $w(z)$. The beam size was quantified as the inverse speckle size of single-shot SAXS patterns taken at various lens positions using 10 nm Vycor. The data were fitted with the Gaussian beam width equation using the listed parameter values.

In this experiment, we wanted to use the speckle pattern to study whether an XFEL beam’s quality is comparable to that of a Gaussian laser beam. Taking the entire range of motor positions, we first made a preliminary plot for observing whether the data indeed follows the expected trend. As the motor position changes, we expect the focal point to shift from before the sample to behind it. This translates into a symmetric plot where the illuminating beam decreases to a minimum beam size before increasing again (reflected in Fig. 4.17).

With the help of Figure 4.17, we knew the minima was around the motor position -222. We then sampled across a shorter range of motor values along the Rayleigh regime to better extract the parameters for $w(z)$ with a statistical fit. Choosing the range [-224, -220], we autocorrelated and fitted the size of speckles in 30 new ROIs and used Eq.(4.6) to determine the beam radius.

In the Rayleigh regime, we still observed a minima, albeit the data was less symmetric than expected. In the right half of Figure 4.18, the data appears to follow the trend of a Gaussian beam defined in Eq.(3.1). The data on the left half of the plot exhibit large deviations from the theoretical expectation and can be a sign of temporarily reduced beam quality for the corresponding sets of trains.

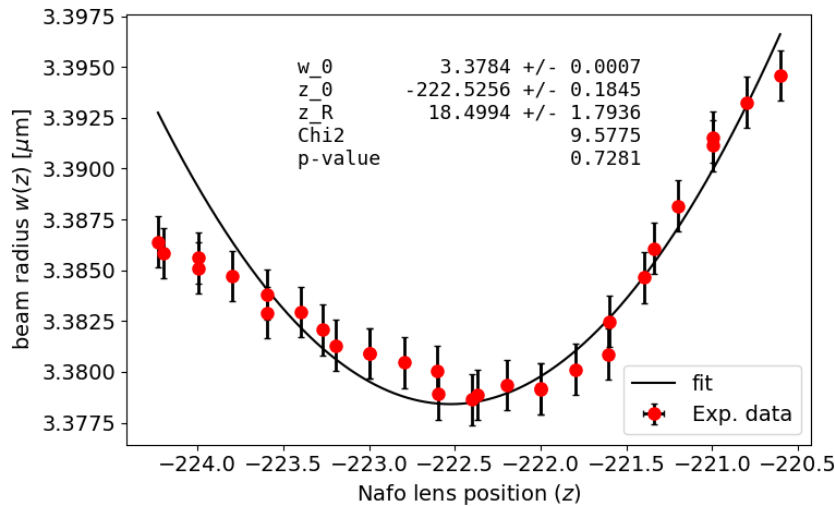


Figure 4.18: Evolution of beam width as a function of lens position $w(z)$ around the Rayleigh regime. The beam width was recovered from the size of speckles in single-shot SAXS patterns taken with 10 nm Vycor. The data were fitted with the Gaussian beam width equation using the listed parameter values.

If the deviations are in fact a reflection of beam quality deterioration, then we can speculate that the cause is similar to how intracavity distortions cause beam quality deterioration in lasers [41]. Beam quality can deteriorate from aberrations in optical elements along the photon tunnel, optics or experimental hutch; or distortion of beam quality that originated in the XFEL gain medium (LINAC or undulator) during the SASE process. If beam quality was not the issue, then alternatively the deviations could be an issue related to poor fitting in our data analysis scripts, although this seems less likely as the analysis was done with an automated program and the right half of the data provided expected results. Both points would require further investigation.

To get a better convergence on optimal fitting parameters in Iminuit, we chose to fit Eq.(3.1) to only the right half of all the data points. Since only one ROI for each beam size was used, our data lacks proper sampling. In this case, we manually set the uncertainty in our data to $\pm 0.00125 \mu\text{m}$ for Iminuit to evaluate our fit, which resulted in a χ^2 of 9.5775. With 13 degrees of freedom, that corresponds to a p value of 0.7281. If the deviation in the left half of the data points is a result of instrument distortions or poor fitting, we can assume that XFEL beams indeed possess laser-like beam quality when no instrument defects are present. The minimum beam radius w_0 was found to be $(3.2784 \pm 0.0007) \mu\text{m}$, and the Rayleigh length is $\approx (1.9 \pm 0.2)$ mm.

In both simulation and experimental cases, we were able to successfully demonstrate the inverse relationship between incident radiation beam size and the resultant speckle size. Starting with a basic SAXS pattern simulation for 2D samples, we obtained a scattering intensity that was compared to a 3D scattering model for monodispersed hard-spheres. While the 3D model was able to fit the first oscillation of the scattering intensity, there were major differences (damping and increased periodicity) in the simulated data that were attributed to the 2D and pixilated nature of our simulation.

Experimental SAXS patterns for monodisperse hard spheres were taken and fitted to further develop an intuitive understanding of the similarities and differences in theoretical and experimental data. While simulations are able to provide a visual guide of what is expected, experimental results often include artifacts, such as noise and smearing that defer from expectation. Having both to compare allows researchers to distinguish which features come from the interactions of interest and which from experimental limitations. In our case, while it is likely that there is a small degree of polydispersity in the LUDOX[®] sample, we concluded that the main difference between the theoretical and experimental SAXS intensities was a result of instrument smearing.

The autocorrelation function's central peak indeed revealed information regarding the speckle size, and we were able to successfully characterise this size with the FWHM of a fitted Gaussian. Upon characterising the speckles, we investigated the focusing properties of XFEL beams by assuming the Rayleigh formalism in the evolution of the beam size with optical focusing. By analysing the speckle size, we were able to characterise how the beam size changed with the use of a nano-focusing lens. Fitting the Gaussian beam size function to the acquired data, we provided evidence that supports the notion that XFEL beams are Gaussian and diffraction limited in nature under the condition that no internal distortions occur before scattering. More so, we demonstrated how one can expand on speckle analysis to study a large variety of experimental parameters related to X-ray scattering.

The main challenge manifested in the peak fitting process of Vycor. In order to fit the central peak, the large background pedestal as a result of the scattering structure

of the sample had to be subtracted. Without an average autocorrelation function $\langle \Gamma_I \rangle$, using $\Gamma_{\langle I \rangle}$ to subtract the background results in fluctuations on either side of the central peak. This becomes an obstacle, especially for delta-like central peaks as our defined Gaussian function struggles to fit accurately in those cases. Therefore, given the time, one should always use averages: $\langle \Gamma_I \rangle$ and $\Gamma_{\langle I \rangle}$ to analyse the spatial autocorrelation of speckle patterns.

Having gained some insight into how simulations can aid in experimental preparation and analysis, it would be beneficial to refine our 2D simulation into producing 3D results as a follow-up project. Obtaining beam time at large-scale facilities such as EuXFEL is competitive and valuable, so one should utilise all resources to ensure quality experimental data is taken. With a scattering pattern simulation, one can familiarise themselves with the expected results or vary parameters to find the optimal experimental configuration for the best results.

As a final note, it would be interesting to demonstrate how DLS analysis techniques are applied in the X-ray regime in XPCS to study the dynamics of our LUDOX[®] sample. So far, we investigated how static speckles can be used to profile XFEL beams. With XPCS, we can study the Brownian motion of our nanoparticles by noting the spatial evolution of speckles in the detector plane over time. XPCS is used mostly to study the dynamics of a sample but is also able to provide information regarding the sample itself, like a secondary measurement of the particle radius, for example.

With the continuation of forefront speckle characterisation, we hope that refined methods of photon correlation experiments can provide a deeper understanding of the dynamical behaviour in soft and condensed matter, visible only with X-rays. A well characterised relationship between speckle and beam size should also aid in the profiling and conditioning of various scattering experiments to simplify and optimize the process of acquiring scientific data.

- [1] Philip Willmott PhD. *An Introduction to Synchrotron Radiation: Techniques and Applications*. en. Google-Books-ID: nEyMDwAAQBAJ. John Wiley & Sons, Mar. 2019. ISBN: 978-1-119-28038-5.
- [2] Anders Madsen, Andrei Fluerasu, and Beatrice Ruta. “Structural Dynamics of Materials Probed by X-Ray Photon Correlation Spectroscopy”. en. In: *Synchrotron Light Sources and Free-Electron Lasers: Accelerator Physics, Instrumentation and Science Applications*. Ed. by Eberhard J. Jaeschke *et al.* Cham: Springer International Publishing, 2016, pp. 1617–1641. ISBN: 978-3-319-14394-1. DOI: 10.1007/978-3-319-14394-1_29. URL: https://doi.org/10.1007/978-3-319-14394-1_29 (visited on 01/23/2023).
- [3] C. Suryanarayana and M. Grant Norton. *X-Ray Diffraction: A Practical Approach*. en. Google-Books-ID: u7EZRnw3_TgC. Springer Science & Business Media, June 1998. ISBN: 978-0-306-45744-9.
- [4] Des McMorro and Jens Als-Nielsen. *Elements of Modern X-ray Physics*. en. Google-Books-ID: rlqlboWlTRMC. John Wiley & Sons, Apr. 2011. ISBN: 978-1-119-97015-6.
- [5] A. Madsen *et al.* “Materials Imaging and Dynamics (MID) instrument at the European X-ray Free-Electron Laser Facility”. en. In: *Journal of Synchrotron Radiation* 28.2 (Mar. 2021), pp. 637–649. ISSN: 1600-5775. DOI: 10.1107/S1600577521001302. URL: <https://scripts.iucr.org/cgi-bin/paper?S1600577521001302> (visited on 01/23/2023).
- [6] Henry Chapman *et al.* “Ultrafast Coherent Diffraction Imaging with X-ray Free-Electron Lasers”. In: *28th International Free Electron Laser Conference, FEL 2006* (Jan. 2006).
- [7] Nanshun Huang *et al.* “Features and futures of X-ray free-electron lasers”. English. In: *The Innovation* 2.2 (May 2021). Publisher: Elsevier. ISSN: 2666-6758. DOI: 10.1016/j.xinn.2021.100097. URL: [https://www.cell.com/the-innovation/abstract/S2666-6758\(21\)00022-9](https://www.cell.com/the-innovation/abstract/S2666-6758(21)00022-9) (visited on 03/27/2023).

- [8] Joseph W. Goodman. *Speckle Phenomena in Optics: Theory and Applications*. en. Google-Books-ID: TynXEcS0DncC. Roberts and Company Publishers, 2007. ISBN: 978-0-9747077-9-2.
- [9] M. Brunel *et al.* “Determination of the Size of Irregular Particles Using Interferometric Out-of-Focus Imaging”. In: *International Journal of Optics* 2014 (Jan. 2014), p. 143904. DOI: 10.1155/2014/143904.
- [10] *Bunch-by-bunch beam size measurement during injection at Shanghai Synchrotron Radiation Facility* | SpringerLink. URL: <https://link.springer.com/article/10.1007/s41365-018-0420-2> (visited on 05/09/2023).
- [11] M. Sutton *et al.* “Observation of speckle by diffraction with coherent X-rays”. en. In: *Nature* 352.6336 (Aug. 1991). Number: 6336 Publisher: Nature Publishing Group, pp. 608–610. ISSN: 1476-4687. DOI: 10.1038/352608a0. URL: <https://www.nature.com/articles/352608a0> (visited on 03/27/2023).
- [12] Eberhard Spiller. *Soft X-ray Optics*. en. Google-Books-ID: khnchMG2kdwC. SPIE Press, 1994. ISBN: 978-0-8194-1654-4.
- [13] Tim Salditt and Markus Osterhoff. “X-ray Focusing and Optics”. en. In: *Nanoscale Photonic Imaging*. Ed. by Tim Salditt, Alexander Egner, and D. Russell Luke. Topics in Applied Physics. Cham: Springer International Publishing, 2020, pp. 71–124. ISBN: 978-3-030-34413-9. DOI: 10.1007/978-3-030-34413-9_3. URL: https://doi.org/10.1007/978-3-030-34413-9_3 (visited on 01/22/2023).
- [14] *ScatteringProcess*. URL: https://xdb.lbl.gov/Section3/Sec_3-1.html (visited on 04/04/2023).
- [15] Bipin K. Agarwal. “Scattering of X-Rays”. en. In: *X-Ray Spectroscopy: An Introduction*. Ed. by Bipin K. Agarwal. Springer Series in Optical Sciences. Berlin, Heidelberg: Springer, 1991, pp. 195–206. ISBN: 978-3-540-38668-1. DOI: 10.1007/978-3-540-38668-1_5. URL: https://doi.org/10.1007/978-3-540-38668-1_5 (visited on 01/20/2023).
- [16] J. H. Hubbell, H. A. Gimm, and I. Øverbø. “Pair, Triplet, and Total Atomic Cross Sections (and Mass Attenuation Coefficients) for 1 MeV-100 GeV Photons in Elements Z=1 to 100”. In: *Journal of Physical and Chemical Reference Data* 9 (Oct. 1980). ADS Bibcode: 1980JPCRD...9.1023H, pp. 1023–1148. ISSN: 0047-2689. DOI: 10.1063/1.555629. URL: <https://ui.adsabs.harvard.edu/abs/1980JPCRD...9.1023H> (visited on 04/04/2023).
- [17] *Beamlines & accelerators*. en-US. Nov. 2021. URL: <https://www.maxiv.lu.se/beamlines-accelerators/> (visited on 05/16/2023).

- [18] Rafael Abela *et al.* *XFEL: The European X-Ray Free-Electron Laser - Technical Design Report*. Journal Abbreviation: DESY Report 2006-097 Publication Title: DESY Report 2006-097. July 2006. ISBN: 978-3-935702-17-1. DOI: 10.3204/DESY_06-097.
- [19] M. V. Kovalchuk and A. E. Blagov. “European X-ray Free-Electron Laser”. en. In: *Crystallography Reports* 67.5 (Oct. 2022), pp. 631–675. ISSN: 1562-689X. DOI: 10.1134/S1063774522050066. URL: <https://doi.org/10.1134/S1063774522050066> (visited on 04/08/2023).
- [20] Orazio Svelto. “Solid-State, Dye, and Semiconductor Lasers”. en. In: *Principles of Lasers*. Ed. by Orazio Svelto. Boston, MA: Springer US, 2010, pp. 375–430. ISBN: 978-1-4419-1302-9. DOI: 10.1007/978-1-4419-1302-9_9. URL: https://doi.org/10.1007/978-1-4419-1302-9_9 (visited on 04/13/2023).
- [21] Anders Madsen *et al.* *Technical Design Report: Scientific Instrument MID*. English. XFEL.EU Technical Report. 2013.
- [22] A. James Stonehouse. *Physics and chemistry of beryllium*. Tech. rep. Elmore, Ohio: Materion Beryllium & Composites, Oct. 1985, p. 14. URL: <https://materion.com/-/media/files/beryllium/beryllium-materials/mb-003physicsandchemistryofberyllium.pdf>.
- [23] V. Kohn, I. Snigireva, and A. Snigirev. “Diffraction theory of imaging with X-ray compound refractive lens”. en. In: *Optics Communications* 216.4 (Feb. 2003), pp. 247–260. ISSN: 0030-4018. DOI: 10.1016/S0030-4018(02)02285-X. URL: <https://www.sciencedirect.com/science/article/pii/S003040180202285X> (visited on 03/27/2023).
- [24] L. D. Dickson. “Characteristics of a propagating gaussian beam”. eng. In: *Applied Optics* 9.8 (Aug. 1970), pp. 1854–1861. ISSN: 1559-128X. DOI: 10.1364/AO.9.001854.
- [25] G. Geloni *et al.* “Coherence properties of the European XFEL”. en. In: *New Journal of Physics* 12.3 (Mar. 2010), p. 035021. ISSN: 1367-2630. DOI: 10.1088/1367-2630/12/3/035021. URL: <https://dx.doi.org/10.1088/1367-2630/12/3/035021> (visited on 03/08/2023).
- [26] *Light - Young's double-slit experiment | Britannica*. en. URL: <https://www.britannica.com/science/light/Youngs-double-slit-experiment> (visited on 04/14/2023).
- [27] J. S. Blakemore. *Solid State Physics*. en. Google-Books-ID: yLwIYiWoOVYC. Cambridge University Press, Dec. 1985. ISBN: 978-0-521-31391-9.

- [28] Brad Osgood. *Lectures on the Fourier Transform and Its Applications*. English. Vol. 33. Stanford, CA: Stanford University, 2019. ISBN: 978-1-4704-4191-3.
- [29] *Small-angle X-ray and neutron scattering* | *Nature Reviews Methods Primers*. URL: <https://www.nature.com/articles/s43586-021-00064-9> (visited on 04/17/2023).
- [30] Sooheyong Lee *et al.* “Single shot speckle and coherence analysis of the hard X-ray free electron laser LCLS”. EN. In: *Optics Express* 21.21 (Oct. 2013). Publisher: Optica Publishing Group, pp. 24647–24664. ISSN: 1094-4087. DOI: 10.1364/OE.21.024647. URL: <https://opg.optica.org/oe/abstract.cfm?uri=oe-21-21-24647> (visited on 05/15/2023).
- [31] Aschkan Allahgholi *et al.* “The Adaptive Gain Integrating Pixel Detector at the European XFEL”. In: *Journal of Synchrotron Radiation* 26.1 (Jan. 2019), pp. 74–82. ISSN: 1600-5775. DOI: 10.1107/S1600577518016077. URL: <http://scripts.iucr.org/cgi-bin/paper?S1600577518016077> (visited on 01/23/2023).
- [32] VYCOR® Code 7913 | *Heat resistant 96% silica glass*. URL: <https://www.pgo-online.com/intl/vycor.html> (visited on 05/16/2023).
- [33] P A Bromiley. “Products and Convolutions of Gaussian Probability Density Functions”. en. In: ().
- [34] Pauli Virtanen *et al.* “SciPy 1.0: fundamental algorithms for scientific computing in Python”. en. In: *Nature Methods* 17.3 (Mar. 2020). Number: 3 Publisher: Nature Publishing Group, pp. 261–272. ISSN: 1548-7105. DOI: 10.1038/s41592-019-0686-2. URL: <https://www.nature.com/articles/s41592-019-0686-2> (visited on 05/16/2023).
- [35] Heloisa Nunes Bordallo. *Chapter 4: Small Angle Scattering, Experimental X-ray Physics*. University of Copenhagen, Feb. 2022.
- [36] Dr Moloi Teboho. *Spherical Bessel functions*. arXiv:2102.02634 [math]. Feb. 2021. DOI: 10.48550/arXiv.2102.02634. URL: <http://arxiv.org/abs/2102.02634> (visited on 10/21/2022).
- [37] S. R. Aragón and R. Pecora. “Theory of dynamic light scattering from polydisperse systems”. In: *The Journal of Chemical Physics* 64.6 (Mar. 1976). Publisher: American Institute of Physics, pp. 2395–2404. ISSN: 0021-9606. DOI: 10.1063/1.432528. URL: <https://aip.scitation.org/doi/10.1063/1.432528> (visited on 01/19/2023).

- [38] D. L. Abernathy *et al.* “Small-Angle X-ray Scattering Using Coherent Undulator Radiation at the ESRF”. en. In: *Journal of Synchrotron Radiation* 5.1 (Jan. 1998). Number: 1 Publisher: International Union of Crystallography, pp. 37–47. ISSN: 0909-0495. DOI: 10.1107/S0909049597015835. URL: [//scripts.iucr.org/cgi-bin/paper?he0220](http://scripts.iucr.org/cgi-bin/paper?he0220) (visited on 01/19/2023).
- [39] *Polydispersity & Orientational Distributions*. Documentation. 2021. URL: <https://www.sasview.org/docs/user/qtgui/Perspectives/Fitting/pd/polydispersity.html> (visited on 05/02/2023).
- [40] Steve King. *Assessing Fit Quality*. Documentation. 2019. URL: https://www.sasview.org/docs/user/qtgui/Perspectives/Fitting/residuals_help.html (visited on 05/04/2023).
- [41] Rüdiger Paschotta. “Beam quality deterioration of lasers caused by intracavity beam distortions”. EN. In: *Optics Express* 14.13 (June 2006). Publisher: Optica Publishing Group, pp. 6069–6074. ISSN: 1094-4087. DOI: 10.1364/OE.14.006069. URL: <https://opg.optica.org/oe/abstract.cfm?uri=oe-14-13-6069> (visited on 05/11/2023).
- [42] Puthusserickal A. Hassan, Suman Rana, and Gunjan Verma. “Making Sense of Brownian Motion: Colloid Characterization by Dynamic Light Scattering”. In: *Langmuir* 31.1 (Jan. 2015). Publisher: American Chemical Society, pp. 3–12. ISSN: 0743-7463. DOI: 10.1021/1a501789z. URL: <https://doi.org/10.1021/1a501789z> (visited on 05/06/2023).

7.1 Github repository

Python script used to simulate and analyse the Fourier transform scattering pattern of a monodispersed nanoparticle sample can be found at:

<https://github.com/christineandersson/Speckle-Simulation>

Python script used to access and analyse experimental data taken from EuXFEL can be found at:

<https://github.com/christineandersson/XFEL-speckle-analysis>

7.2 Calculating the diffusion coefficient of 25 nm LUDOX[®]

For a system of nanoparticles suspended in a liquid at thermal equilibrium, we can assume any inter-particle interactions to be negligible. The change in the particle's position is then expected to follow a stochastic process known as Brownian motion - where the pattern of motion is completely random due to the surrounding many-particle interactions causing no net direction of force.

For 25 nm SiO₂ particles suspended in water, the mean translational diffusion coefficient, D in the Stokes-Einstein equation for Brownian motion is given by [42]:

$$D = \frac{k_B T}{6\pi\eta r}, \quad (7.1)$$

where k_B is the Boltzmann constant, T the temperature of the system, η the viscosity of the liquid suspension and r the radius of the nanoparticle.

The conditions of LUDOX[®] at room temperature ($r = 25$ nm, $T = 295$ K, $\eta = 0.9544$ mPa·s) then result in a diffusion coefficient of:

$$D = \frac{(1.38 \times 10^{-23} \text{ J} \cdot \text{K}^{-1})(295 \text{ K})}{6\pi(0.9544 \times 10^{-3} \text{ kgm}^{-1}\text{s}^{-1})(25 \times 10^{-9} \text{ m})} = 0.905 \times 10^{-11} \text{ m}^2/\text{s}.$$

The mean square displacement, \bar{x}^2 , of the particle is related to the timescale and Diffusion coefficient by $\bar{x}^2 = 6Dt$ [2], which for a mean square displacement equivalent to the diameter of a particle (50 nm) gives us a characteristic timescale of:

$$\left(\frac{2\pi}{50 \text{ nm}}\right)^2 \times 6D = \frac{1}{t} \iff t \approx 1.2 \times 10^{-6} \text{ s}.$$

7.3 Calculating the electron density of SiO₂ and H₂O

To find the electron density of a molecule, the following equation can be used:

$$N_e \times \frac{1}{M} \times \rho \times A_g,$$

where N_e is the number of electrons, M the molar mass, ρ the mass density and A_g is Avogadro's constant. To double check the consistency of this equation, we can look at the units:

$$\left[\frac{\text{electrons}}{1}\right] \times \left[\frac{\text{mol}}{g}\right] \times \left[\frac{g}{\text{\AA}^3}\right] \times \left[\frac{1}{\text{mol}}\right] = \left[\frac{\text{electrons}}{\text{\AA}^3}\right]$$

For SiO₂, there are 30 electrons per molecule and a mass density of $2.65 \times 10^{-24} \text{ g/\AA}^3$. The molar mass of SiO₂ is 60.08 g/mol, which gives us an electron density of:

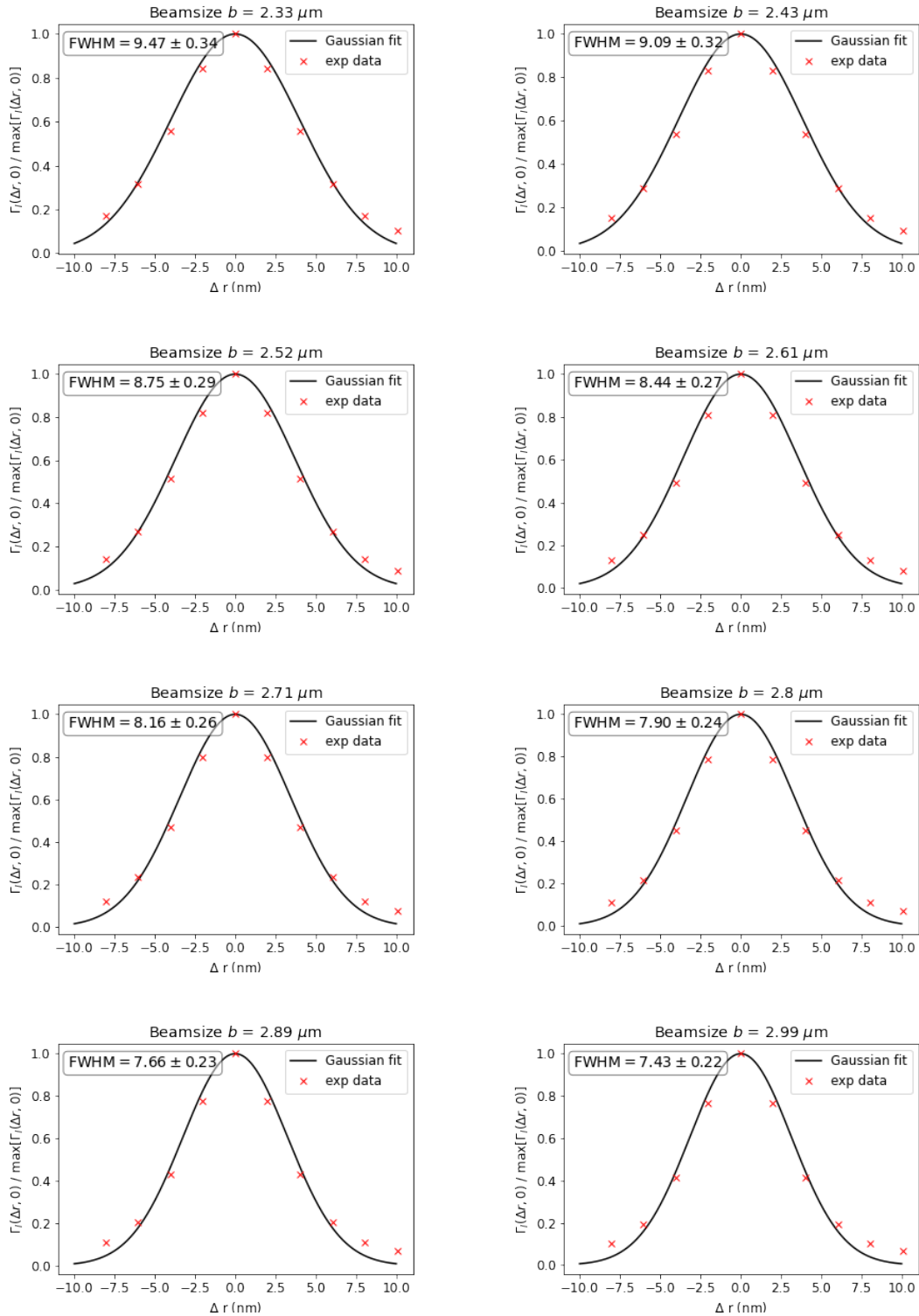
$$30 \times \left(\frac{1}{60.08 \text{ g mol}^{-1}}\right) \times (2.65 \times 10^{-24} \text{ g \AA}^{-3}) \times (6.02214 \times 10^{23} \text{ mol}^{-1}) \\ \approx 0.797 \text{ electrons / \AA}^3$$

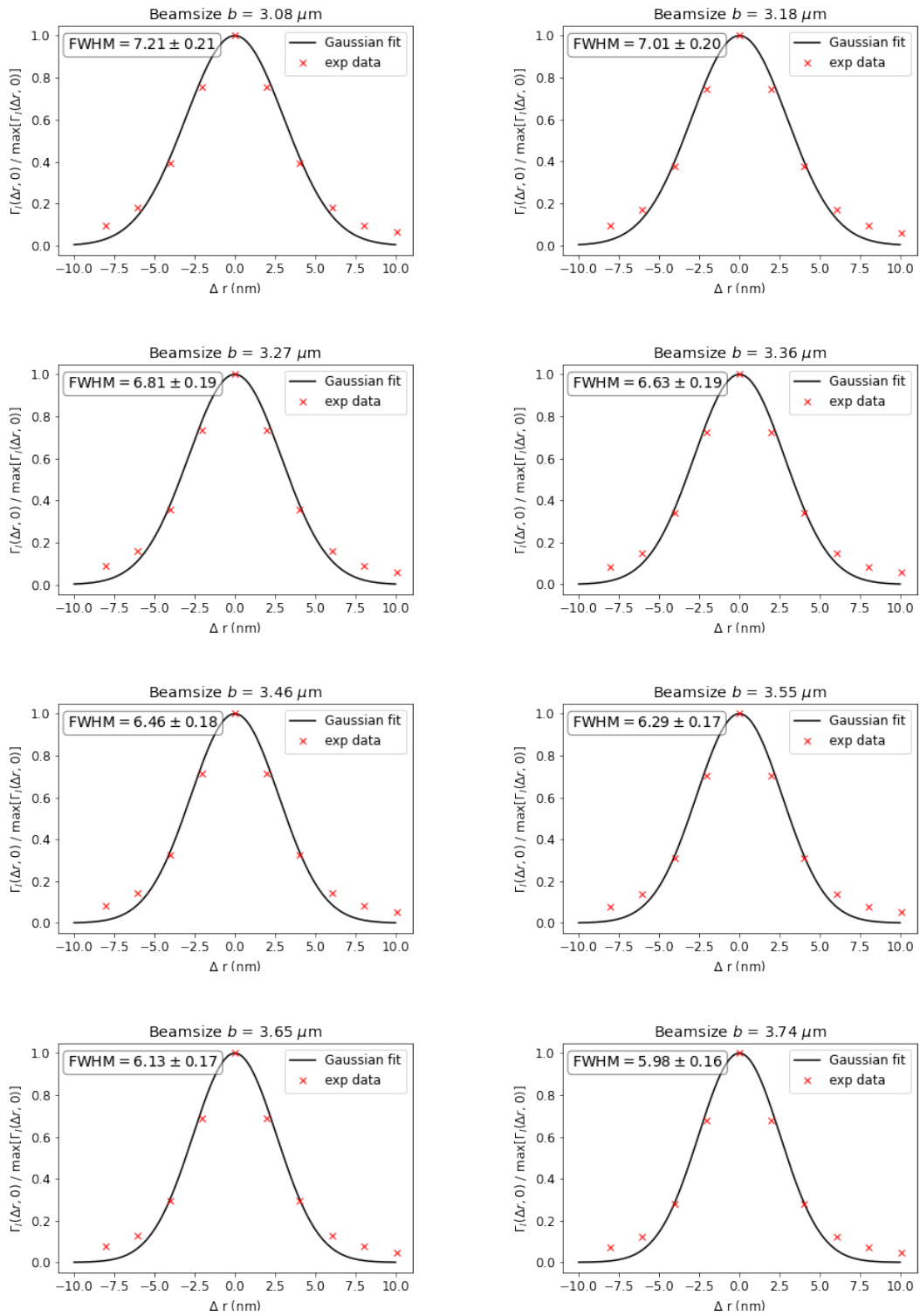
The same logic can be applied to H₂O, which has 10 electrons per molecule and a density of $1 \times 10^{-24} \text{ g/\AA}^3$. The molar mass of water is 18.02 g/mol, which results in an electron density of:

$$10 \times \left(\frac{1}{18.02 \text{ g mol}^{-1}}\right) \times (1 \times 10^{-24} \text{ g \AA}^{-3}) \times (6.02214 \times 10^{23} \text{ mol}^{-1}) \\ \approx 0.334 \text{ electrons / \AA}^3$$

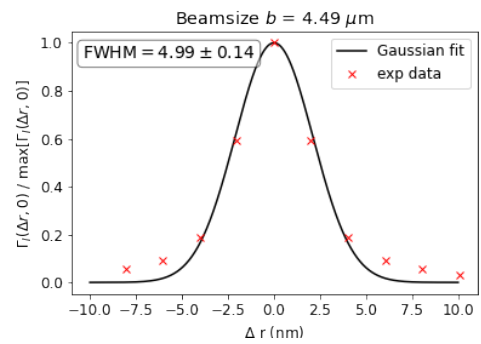
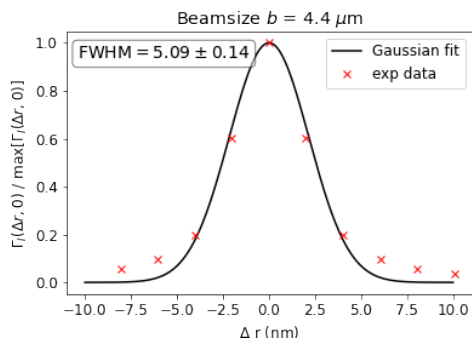
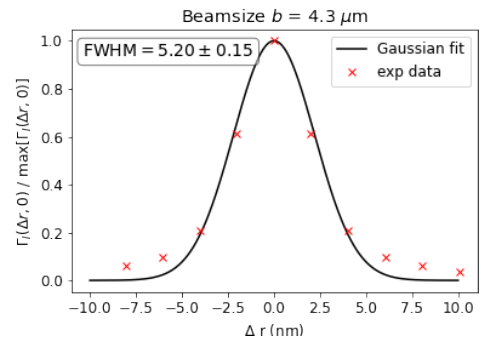
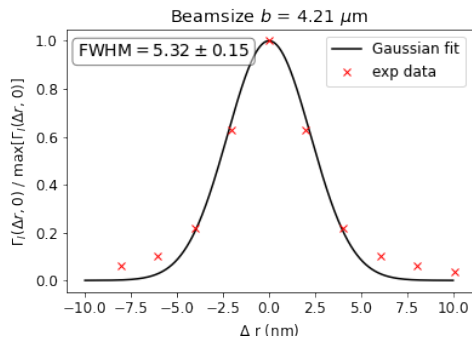
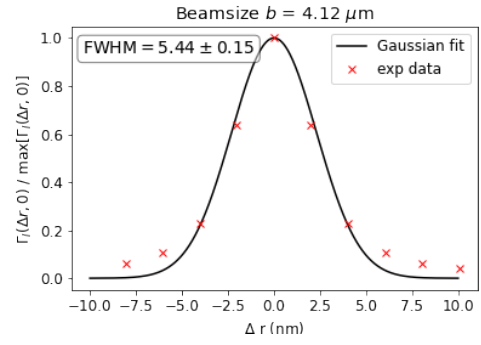
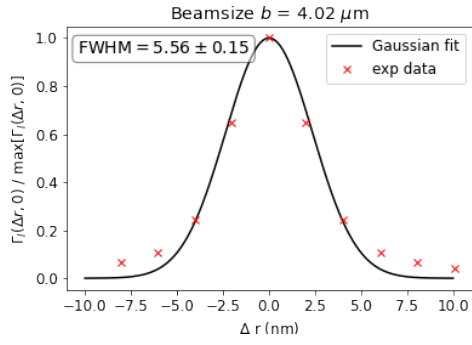
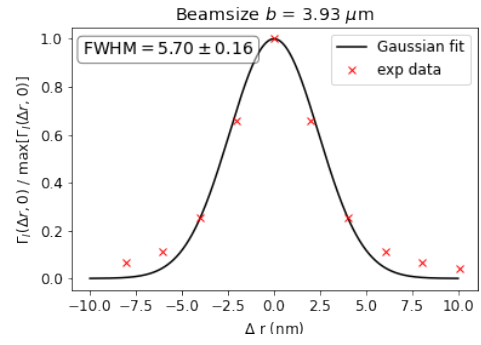
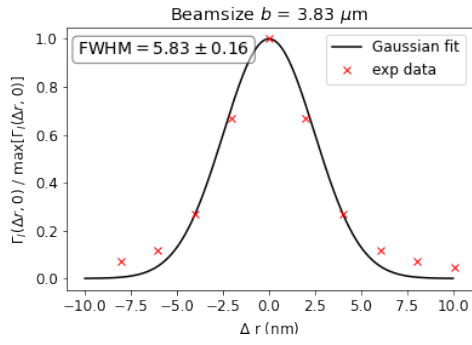
From the electron densities calculated, we can tell that materials made of SiO_2 have approximately 2.4 times higher electron density than its surrounding environment of H_2O .

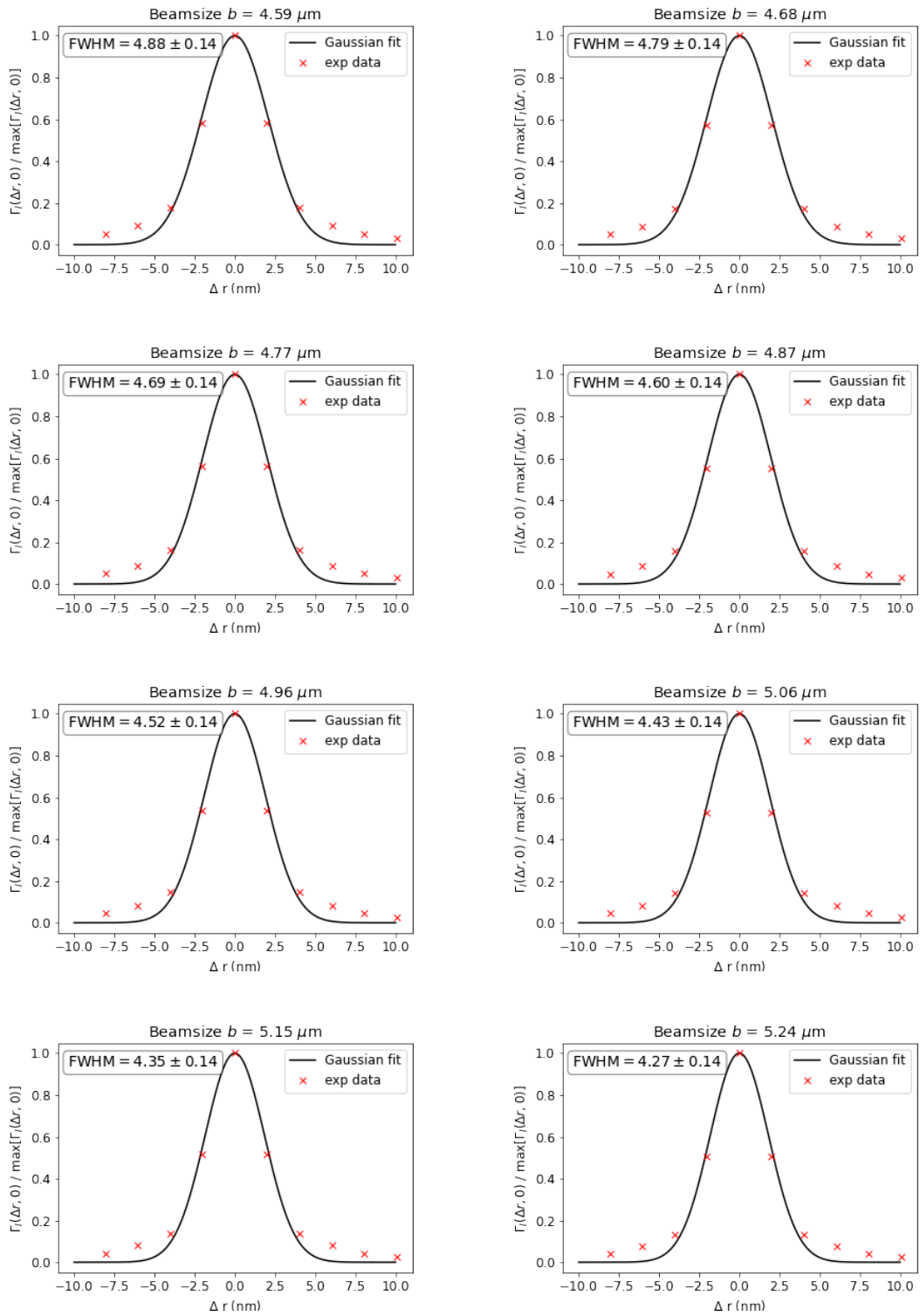
7.4 Fitting of the central peak feature in the y-cut autocorrelation functions for the simulated speckle pattern ROI.



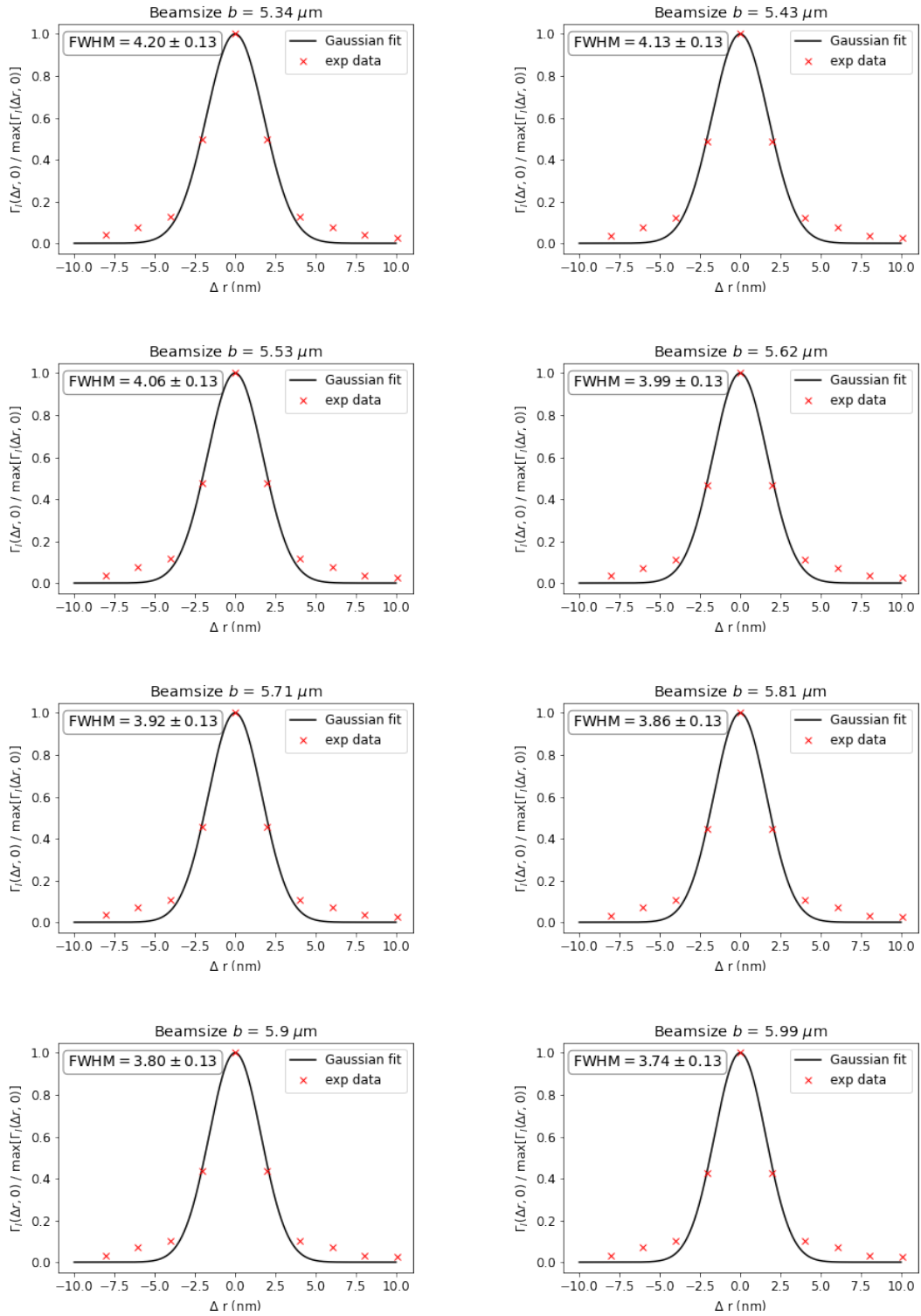


7.4 Fitting of the central peak feature in the y-cut autocorrelation functions for the simulated speckle pattern





7.4 Fitting of the central peak feature in the y-cut autocorrelation functions for the simulated speckle pattern



7.4 Fitting of the central peak feature in the y-cut autocorrelation functions for the simulated speckle pattern

7.5 Sasview fitting with various hard-sphere models for 25 nm LUDOX[®] nanoparticles.

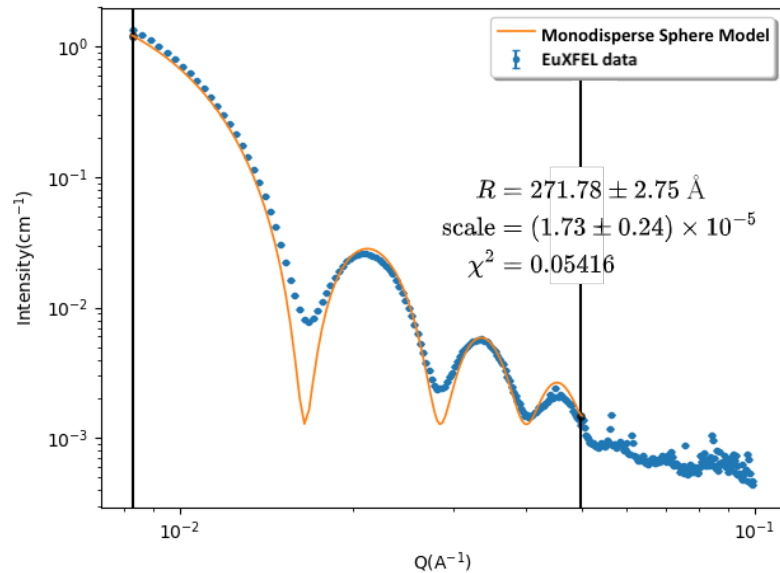


Figure 7.1: Sasview fitting of the scattering intensity of 25 nm LUDOX[®] acquired at the European XFEL with a monodisperse sphere model.

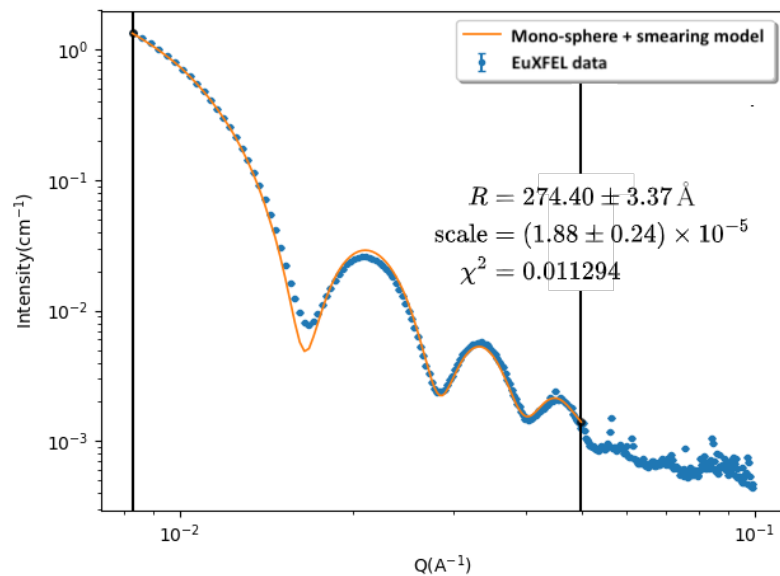


Figure 7.2: Sasview fitting of the scattering intensity of 25 nm LUDOX[®] acquired at the European XFEL with a monodisperse sphere model including $dQ/Q = 5\%$ instrument resolution smearing.

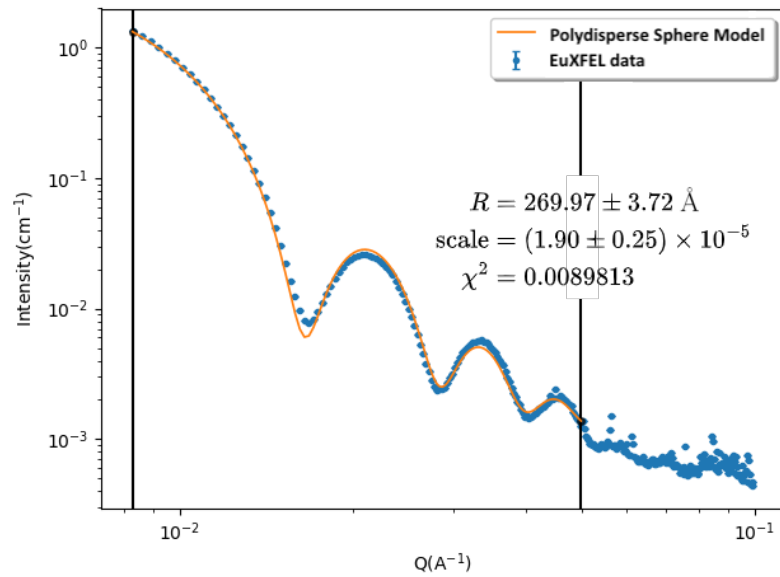


Figure 7.3: Sasview fitting of the scattering intensity of 25 nm LUDOX[®] acquired at the European XFEL with a Gaussian polydisperse hard sphere model ($PD: 0.06 \pm 0.01$) Å.